Nuclear Spins as Quantum Testbeds: Singlet States, Quantum Correlations, and Delayed-choice Experiments

A thesis

Submitted in partial fulfillment of the requirements

Of the degree of

Doctor of Philosophy

By

Soumya Singha Roy

20083009

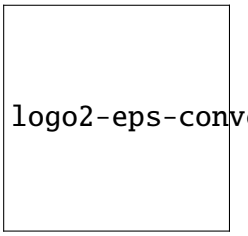

INDIAN INSTITUTE OF SCIENCE EDUCATION AND RESEARCH PUNE

August, 2012

Certificate

Certified that the work incorporated in the thesis entitled "*Nuclear Spins as Quantum Testbeds: Singlet States, Quantum Correlations, and Delayed-choice Experiments*", submitted by *Soumya Singha Roy* was carried out by the candidate, under my supervision. The work presented here or any part of it has not been included in any other thesis submitted previously for the award of any degree or diploma from any other University or institution.

Date **Dr. T. S. Mahesh**

Declaration

I declare that this written submission represents my ideas in my own words and where others' ideas have been included, I have adequately cited and referenced the original sources. I also declare that I have adhered to all principles of academic honesty and integrity and have not misrepresented or fabricated or falsified any idea/data/fact/source in my submission. I understand that violation of the above will be cause for disciplinary action by the Institute and can also evoke penal action from the sources which have thus not been properly cited or from whom proper permission has not been taken when needed.

Date **Soumya Singha Roy**

Roll No.- 20083009

Acknowledgement

This thesis would have not been possible without the help and support by many individuals whom I met during my PhD life at IISER Pune. I have been very privileged to have so many wonderful friends and collaborators.

First of all, I am grateful to my advisor Dr. T. S. Mahesh for teaching me everything about NMR and Quantum Information Processing starting from the scratch. His cheerful guidance and deep understanding in NMR-QIP are the driving forces behind this thesis. Being his first PhD student, I consider myself to be very fortunate to get all of his support, care and affection.

I would like to thank Dr. Vikram Athalye for his valuable set of lectures which ultimately led to a fruitful collaborative work. I thank Prof. G. S. Agarwal for some constructive discussions with him and visiting us in spite of his busy schedule. I am thankful to Prof. Apoorva Patel for useful discussions and collaboration. Very special thanks to Prof. Anil Kumar for his great support and insightful conversations on various scientific problems and my future career path.

I thank all the members of NMR Research Center -past and present- with whom I have worked. It's been a great pleasure working with Abhishek (whom we fondly call 'Shuklaji') for all his 'complicated' queries and thoughtful discussions that I had with him. His famous 'I am not saying this, but I am saying that' is really unforgettable. It was highly exciting to work with Hemant who became an integral part of the NMR center ever since he joined the lab. Discussions on 'Quantum weirdness' were always intriguing with Manvendra. Working with Swathi was interesting because of her thorough theoretical understandings. Short stay of Philipp left many sweet memories of the discussions that I had with him. Discussions with Sheetal and Abhijeet were interesting and that actually made me learn many aspects of NMR and Quantum Computing. I also thank Pooja for her organized way of managing the spectrometers for years. Sachin was always there to look after the spectrometers and he made sure that it's up all the time.

I thank my RAC members- Dr. A. Bhattacharyay, Dr. T. G. Ajitkumar, and Dr. K. Gopalakrishnan for all their support. I also thank Dr. R. G. Bhat, Dr. V. G. Anand, Dr. H. N. Gopi, for all those help and affection. I am thankful to Prof. K. N. Ganesh for providing all the necessary experimental facilities in the lab. I thank Dr. V. S. Rao for all his help whenever I needed, be it academic or non-academic. I would like to thank CSIR and IISER for the graduate scholarships that I received during my PhD.

Life outside lab was also highly enjoyable for many many friends and I thank them all. I thank all my friends in Physics department, especially my 2008 batch mates for all their support and good times we had together. Arthur's casual approach and Murthy's 'mass' approach created a funny contrast that I had thoroughly enjoyed all these years. Mayur always surprises me with his witty comments and jokes. Arun, Kanika, Padma, Ramya, and Resmi provided jovial company always. I thank all my friends in Chemistry department for helping me with many chemical compounds whenever I needed.

I thank Anurag, Harsha, JP, and Amar for all those adventurous weekend treks and cheerful company. Dinner table was always full of noise, argument, and fun because of Biplab, Abhigyan, and Dada and I thank them all for making it so fascinating. Dada also has been my very close friend and room-mate for all these years.

I thank all my long-time and long-distance friends- Sudipta, Diganta, Kalyan, Nandan, Swarup and Souravda for their support and encouragement. Conversations were always cheerful and motivating with them.

My research career would have not been possible without the active support of my family. I thank my mother, father and sister for their love, support and encouragement throughout all the time.

Contents

List of Figures

List of Publications

1. S. S. Roy and T. S. Mahesh,
Density Matrix Tomography of Singlet States,
J. Magn. Reson. **206**, 127 (2010).

2. S. S. Roy and T. S. Mahesh,
Initialization of NMR Quantum Registers using Long-Lived Singlet States,
Phys. Rev. A **82**, 052302 (2010).

3. S. S. Roy, T. S. Mahesh, and G. S. Agarwal,
Storing Entanglement of Nuclear Spins via Uhrig Dynamical Decoupling,
Phys. Rev. A **83**, 062326 (2011).

4. V. Athalye, S. S. Roy, and T. S. Mahesh,
Investigation of Leggett-Garg Inequality for Precessing Nuclear Spins,
Phys. Rev. Lett. **107**, 130402 (2011).

5. S. S. Roy, A. Shukla, and T. S. Mahesh,
NMR Implementation of Quantum Delayed-Choice Experiment,
Phys. Rev. A **85**, 022109 (2012)

6. S. S. Roy and T. S. Mahesh,
Study of Electromagnetically Induced Transparency using Long-Lived Singlet States,
arXiv : quant-ph/1103.3386

7. H. Katiyar, S. S. Roy, T. S. Mahesh, and A. Patel,
Evolution of Quantum Discord and its Stability in Two-qubit NMR Systems,
Phys. Rev. A **86**, 012309 (2012)

8. S. S. Roy, M. Sharma, V. Athalye, and T. S. Mahesh,
Experimental Test of Quantum Contextuality in Nuclear Spin Ensembles,
(in preparation).

Abstract

Nuclear Magnetic Resonance (NMR) forms a natural test-bed to perform quantum information processing (QIP) and has so far proven to be one of the most successful quantum information processors. The nuclear spins in a molecule are treated as quantum bits or qubits which are the basic building blocks of a quantum computer.

The long lived singlet state (LLS) has found wide range of applications ever since it was discovered by Carravetta, Johannessen, and Levitt in 2004. Under suitable conditions, singlet states can live up to minutes or about many times of longitudinal relaxation time constant (T1). For the first time, we have exploited the long lifetime of singlet states in NMR to execute several potentially important QIP problems. We were able to prepare high fidelity pseudopure states (PPS) in multi-qubit systems starting from LLS. We developed an efficient scheme of density matrix tomography to study all these quantum states. The tomographic study on LLS shows some interesting results. We performed experiments, where we created all the four Bell states from LLS and then studied the effect of various dynamical decoupling sequences on preserving these states. We found that Uhrig dynamical decoupling sequence is better than CPMG sequence in preserving Bell states for longer duration under suitable conditions.

Nuclear spin systems form convenient platforms for studying various quantum phenomena. We used violation of Leggett-Garg Inequality (LGI) in a two-qubit system to study the transition from quantum to macrorealistic behavior. We observed perfect violation of LGI for time scales which are much small compared to the spin-spin relaxation time scales. However, with the increasing time scales, we notice a gradual transition of spin-states from quantum to classical behavior. This steady arrival of classicality can be attributed to the decoherence process. In a separate experiment we performed quantum delayed choice experiment in nuclear spin ensembles to study the wave-particle duality of quantum states. These set of experiments clearly demonstrate a continuous morphing of the target qubit between particle-like and wave-like behaviors, thus supporting the theoreticians' demand to reinterpret Bohr's complementary principles.

Chapter 1

Density Matrix Tomography of Long Lived Singlet States

The lifetime of nuclear singlet states can be much longer than any other non-equilibrium states under suitable conditions. In section 2.2, we introduced long-lived singlet (LLS) states and it's preparation by standard methods. In section 2.3, we introduced a robust density matrix tomography scheme which is particularly suited to study homonuclear spin systems with small chemical shift differences. In section 2.4, we have applied the tomography scheme to characterize the singlet states under various experimental conditions, revealing interesting features of LLS. This chapter ends with a conclusion given in section 2.5.

1.1 Introduction

The long lifetimes of nuclear spin coherence enables NMR spectroscopists to carry out a variety of spin choreography [**?**, **?**]. Nuclear spin coherences decay over time mainly due to spin-spin relaxation and magnetic field inhomogeneity. Often, coherences are converted into longitudinal nuclear spin orders to study slow dynamical processes. But even the longitudinal spin orders decay toward equilibrium state due to spin-lattice

relaxation. Hence for a typical NMR experiment consisting of preparing and measuring certain correlated spin states, the ultimate time barrier was assumed to be defined by the spin-lattice relaxation time constant T_1 [**?**].

It has recently been demonstrated that there exist certain 'long-lived states' which decay slower than the T_1 values of individual spins [**?**, **?**, **?**, **?**, **?**, **?**, **?**, **?**]. The long lived singlet states (LLS) has found wide range of applications ever since it was discovered by Carravetta, Johannessen, and Levitt in 2004 [**?**]. Overcoming the T_1 barrier has led to several exciting applications in studying slow molecular dynamics and transport processes [**?**, **?**], precise measurements of NMR interactions [**?**], and the transport and storage of hyperpolarized nuclear spin orders [**?**, **?**, **?**, **?**, **?**, **?**].

Bodenhausen and co-workers have demonstrated that the singlet spin-lock can also be achieved by RF modulations which are used in heteronuclear spin-decoupling [**?**]. Detailed theoretical analysis of zero-field singlet states as well as singlet spin-lock have already been provided by Levitt and co-workers [**?**, **?**] and by Karthik et al [**?**]. Recently, long-lived states in multiple-spin systems are also being explored [**?**, **?**].

1.2 Long-lived singlet states

Let us begin with a simplest model consisting of a pair of spin-1/2 nuclei. These two spins are labeled as I^1 and I^2. The free-precession Hamiltonian of this system at laboratory frame can be written as,

$$\mathcal{H} = \omega_1 I_z^1 + \omega_2 I_z^2 + 2\pi J_{12} I^1 \cdot I^2, \tag{1.1}$$

where ω_1 and ω_2 are denoting the resonant frequency of the two spins respectively, whereas J_{12} denotes the spin-spin coupling (J-coupling) between the two spins.

The quantum states of the system can always be expressed with the combination of superposition of Zeeman states, namely $|00\rangle$, $|01\rangle$, $|10\rangle$, $|11\rangle$. Here $|0\rangle$ denotes the angular momentum of $\hbar/2$ along the magnetic field direction ('up' direction) and $|1\rangle$ denotes

the angular momentum of $-\hbar/2$ along the exact opposite direction of the magnetic field ('down' direction). The four Zeeman product states together lead to one singlet state and three triplet states,

$$\begin{aligned} |S_0\rangle &= \frac{|01\rangle - |10\rangle}{\sqrt{2}}, \\ |T_{+1}\rangle &= |00\rangle, \\ |T_0\rangle &= \frac{|01\rangle + |10\rangle}{\sqrt{2}}, \\ |T_{-1}\rangle &= |11\rangle. \end{aligned} \tag{1.2}$$

Singlet states have many different properties compared to its triplet counterparts. Two most important properties are:

(a) Singlet state is anti-symmetric with respect to spin-exchange, whereas triplet states are symmetric.

(b) Singlet state has a zero total nuclear spin angular momentum quantum number $[I^2|S_0\rangle = 0]$, whereas triplet states have non-zero total nuclear spin angular momentum quantum number $[I^2|T_M\rangle = 2|T_M\rangle]$.

In the case of magnetically equivalent nuclear pair, the singlet state and the triplet states form an orthonormal eigenbasis of the internal Hamiltonian $\mathcal{H}_J = 2\pi J I^1 \cdot I^2$. Singlet states can be prepared between two assymetric spins by imposing equivalence condition (either by lifting the sample out of Zeeman field or by applying suitable RF field acting as 'spin-lock'). But, being a zero-quantum coherence, singlet state itself is inaccessible to macroscopic observable directly. The traditional methods by Caravetta et al [**?**], described the way to access the singlet states by breaking its magnetic symmetry to convert into observable single quantum coherences. In this context we may note that, protons in Hydrogen molecule or in water is already in magnetic equivalence, but there is still no way to break the symmetry.

1.2.1 Why singlet state is long lived ?

Any quantum state, deviating from its thermal equilibrium conditions, will return to its stable thermal equilibrium state through a mechanism known as relaxation. Hence it is needless to say that in NMR any observable quantum state is in non-equilibrium condition and that is the reason each state has its own lifetime. There are two major factors behind relaxation, (i) spin-lattice relaxation (T_1) and (ii) spin-spin relaxation (T_2). In majority of the cases T_2 relaxation is much faster than T_1. So the upper limit of the nuclear spin memory is bounded by the T_1 irrespective of any experimental safe guard. However, there are some specialized cases where exceptions can be found, such as in the case of 'parahydrogen', where the spin state isomers lived much longer than T_1 [**?**]. Though the major reasons behind T_1, T_2 relaxation depend on individual molecular property, other controllable parameters such as magnetic field inhomogeneity, temperature fluctuations, sample concentration etc. also contributes to the relaxation mechanism.

Levitt and co-workers have successfully demonstrated [**?**, **?**] that the singlet state lifetime can be made many orders of magnitude longer than T_1 for 'ordinary' molecules in solution state of homonuclear system. Now we will discuss some physics behind this astonishing long-lifetime of singlet states [**?**]. The Hamiltonian for a pair of spins in magnetically equivalent environment is written as bellow:

$$\mathcal{H} = \omega_0 \left(I_z^1 + I_z^2\right) + 2\pi J I^1 \cdot I^2, \tag{1.3}$$

where, $\omega_0 = \gamma B_0$ denotes the Larmor frequency of both (equivalent) the spins and B_0 is the applied static magnetic field. The matrix representation of the Hamiltonian in

singlet-triplet basis can be written [**?**] as follows:

$$\mathcal{H} = \begin{array}{c} \\ \langle S_0| \\ \langle T_{+1}| \\ \langle T_0| \\ \langle T_{-1}| \end{array} \begin{array}{c} \begin{array}{cccc} |S_0\rangle & |T_{+1}\rangle & |T_0\rangle & |T_{-1}\rangle \end{array} \\ \begin{pmatrix} -\frac{3}{2}\pi J & 0 & 0 & 0 \\ 0 & \omega_0 + \frac{1}{2}\pi J & 0 & 0 \\ 0 & 0 & \frac{1}{2}\pi J & 0 \\ 0 & 0 & 0 & -\omega_0 + \frac{1}{2}\pi J \end{pmatrix} \end{array}. \tag{1.4}$$

From the earlier equation it is seen that at zero field ($\omega_0 = 0$), the triplet states are degenerate with same energy eigenvalues ($\frac{1}{2}\pi J$). The energy difference between the singlet and the triplet sates is $2\pi J$ which is independent of the field. Since the Hamiltonian is diagonal, there will not be any mix-up of singlet state population with triplet states' populations [**?**]. However, triplet states among themselves equilibrate quickly. Eventually there will be a singlet-triplet transition resulting in the re-establishment of thermal equilibrium much slower than T_1 relaxation time scale. The time constant for singlet-triplet equilibration is loosely termed as 'singlet lifetime' (T_S) [**?**].

We already know that singlet states are 'antisymmetric' with respect to spin exchange, whereas triplet states are 'symmetric' with respect to the spin exchanges. The major relaxation processes, including intra-molecular dipolar relaxation mechanism, are 'symmetry preserving' in nature. Hence these relaxation mechanisms will not affect the singlet-triplet conversion which requires symmetry transformations. These conditions make singlet states as a 'special' state which is immune to intra-molecular dipolar relaxation, though it is the major reason behind T_1 relaxation [**?**].

Previous discussion shows how necessary it is to get a magnetically equivalent pair of nuclear spins to realize the LLS. We need to create such a magnetically equivalent condition to create and persist in singlet states, but to get signal out of singlet states we need to break the symmetry. In the next paragraphs we will discuss about the techniques for magnetically inequivalent pair of nuclear spins. The Hamiltonian for a pair of

chemically inequivalent nuclei in present of Zeeman field can be written as follows:

$$\begin{aligned}\mathcal{H} &= \omega_1 I_z^1 + \omega_2 I_z^2 + 2\pi J I^1 \cdot I^2 \\ &= \omega_0(1+\delta_1) I_z^1 + \omega_0(1+\delta_2) I_z^2 + 2\pi J I^1 \cdot I^2, \end{aligned} \tag{1.5}$$

where δ_1 and δ_2 are the two chemical shifts of the two spins. The matrix representation of this Hamiltonian in singlet-triplet basis can be expressed as [**?**]:

$$\mathcal{H} = \begin{array}{c} \\ \langle S_0| \\ \langle T_{+1}| \\ \langle T_0| \\ \langle T_{-1}| \end{array} \begin{array}{c} \begin{array}{cccc} |S_0\rangle & |T_{+1}\rangle & |T_0\rangle & |T_{-1}\rangle \end{array} \\ \begin{pmatrix} -\frac{3}{2}\pi J & 0 & \frac{1}{2}\omega_0\Delta\delta & 0 \\ 0 & \omega_0(1+\frac{1}{2}\sum\delta)+\frac{1}{2}\pi J & 0 & 0 \\ \frac{1}{2}\omega_0\Delta\delta & 0 & \frac{1}{2}\pi J & 0 \\ 0 & 0 & 0 & -\omega_0(1+\frac{1}{2}\sum\delta)+\frac{1}{2}\pi J \end{pmatrix} \end{array}, \tag{1.6}$$

where,

$$\sum \delta = \delta_1 + \delta_2, \quad \Delta\delta = \delta_1 - \delta_2. \tag{1.7}$$

In this case, the matrix is not a diagonal matrix, hence the singlet and triplet states are not the eigenstates of this Hamiltonian. The off-diagonal term in the matrix ($\frac{1}{2}\omega_0\Delta\delta$) represents the possible conversion of singlet-triplet transition. This transition is directly dependent on the chemical shift difference between the two spins. Hence, even if we are able to prepare singlet states in an inequivalent pair of nuclei, it will not be long lived till it has some dependency on the chemical shift differences. Still, it gives us a clue to experience long-lived singlet states if somehow the chemical shift difference ($\Delta\delta$) is suppressed [**?**]. In the next subsection we will discuss this method of chemical shift suppression in detail.

1.2.2 Singlet Preparation in NMR

So far we have learn that singlet states can not be observed for magnetically equivalent pair of spins, as it does not give any observable NMR signal, and even for the magneti-

cally inequivalent spin pairs because of the chemical shift difference barrier.

The key to LLS revelation is to switch the magnetic equivalence 'on' and 'off' by some experimental manipulations [**?**]. There are at least two well established procedures to do so - (i) field cycling and (ii) radiofrequency spin-locking [**?**, **?**]. By field cycling method, we can switch-off the magnetic field manually so that magnetic equivalence is established and then once again switch-on the magnetic field to convert into single quantum coherences. The other method (radiofrequency spin-locking) is more practical with least manual work. We will discuss this method in detail.

Getting pure singlet states may be seen as a three step procedure:

(i) Building singlet population.

(ii) Applying spin-lock.

(iii) Singlet detection.

Building singlet population

With the application of suitable *rf* pulses and delays it is possible to create a density matrix operator which represents a part of singlet states in it. The density matrix for a singlet population can be represented by the Cartesian product operator formalism as follows:

$$\begin{aligned} |S_0\rangle\langle S_0| &= \frac{1}{2}\left(|01\rangle - |10\rangle\right)\left(\langle 01| - \langle 10|\right) \\ &= \frac{1}{2}\left(|01\rangle\langle 01| - |10\rangle\langle 01| - |01\rangle\langle 10| + |10\rangle\langle 10|\right) \\ &= \frac{1}{2}\left(I^1_{|0\rangle}I^2_{|1\rangle} - I^1_+I^2_- - I^1_-I^2_+ + I^1_{|1\rangle}I^2_{|0\rangle}\right) \\ &= -\frac{1}{2}\left(I^1_+I^2_- + I^1_-I^2_+\right) - I^1_zI^2_z + \frac{1}{4}\mathbb{1}. \end{aligned} \tag{1.8}$$

The earlier equation shows that singlet populations can be constructed from zero quantum coherences and longitudinal magnetization of both the spins. Hence a little trick with the excitation of zero quantum coherences with appropriate phase can leads us to the singlet populations [**?**]. The following pulse sequence is found [**?**] suitable to

create singlet state populations starting from equilibrium condition.

$$90_0 - \tau_1 - 180_0 - (\tau_1 + \tau_2) - 90_{90} - \tau_3, \tag{1.9}$$

where $\tau_1 = 1/4J$, $\tau_2 = 1/2\Delta\nu$ and $\tau_3 = 1/4\Delta\nu$. J and ν are denoting the spin-spin coupling constant and chemical shift difference in Hz respectively. The 'offset' should be placed at the middle of the two spins for simplification. The above written pulse sequence works as follows :

Initial 90_0 pulse brings the longitudinal magnetization to transverse plane.

$$I_z^1 + I_z^2 \xrightarrow{90_0} -I_y^1 - I_y^2,$$

followed by the spin-echo with only J evolution for the duration of 1/2J :

$$-I_y^1 - I_y^2 \xrightarrow{\tau_1 - 180_0 - \tau_1} 2I_x^1 I_z^2 + 2I_z^1 I_x^2.$$

During the subsequent τ_2 interval, there will be evolution under the isotropic chemical shifts. This delay ($\tau_2 = 1/2\Delta\nu$) is relatively shorter and can be ignored for any significant J-evolution during this time. The product operator formalism goes as follows:

$$2I_x^1 I_z^2 + 2I_z^1 I_x^2 \xrightarrow{\tau_2} 2I_y^1 I_z^2 - 2I_z^1 I_y^2.$$

Now a 90 degree y pulse will bring the density operator into zero quantum coherences.

$$2I_y^1 I_z^2 - 2I_z^1 I_y^2 \xrightarrow{90_{90}} 2I_y^1 I_x^2 - 2I_x^1 I_y^2 = -i(I_+^1 I_-^2 - I_-^1 I_+^2).$$

A further chemical shift evolution required for a phase corrected zero quantum coherence.

$$2I_y^1 I_x^2 - 2I_x^1 I_y^2 \xrightarrow{\tau_3} -2I_x^1 I_x^2 - 2I_y^1 I_y^2 = -(I_+^1 I_-^2 + I_-^1 I_+^2).$$

This may be rewritten as follows:

$$\begin{aligned} -I_+^1 I_-^2 - I_-^1 I_+^2 &= -|01\rangle\langle 10| - |10\rangle\langle 01| \\ &= |S_0\rangle\langle S_0| - |T_0\rangle\langle T_0|. \end{aligned} \tag{1.10}$$

Hence from the above calculations it is seen that the resulting density operator is in fact combination of the singlet state and one of the triplet states' population. Now our aim is to filter out the singlet state from the singlet-triplet population distribution. This can be done by radio frequency spin locking as discussed below in detail.

Radio frequency spin-lock

A spin-lock is a low power on-resonant continuous radio frequency pulse along the spin magnetization in transverse plane. This low frequency *rf* pulse keeps the magnetization from precessing in transverse plane. Hence this pulse can be used as a possible way to suppress the chemical shift differences. It is popularly known as a 'spin-lock' as it arrests the spin precession.

The duration of the spin-lock may last for several minutes, triggering the possibility of severe probe damage. Hence one must be careful to select the *rf* spin-lock power and duration. There are two basic kinds of spin-lock. (i) Unmodulated spin-lock, and (ii) modulated spin-lock.

(i) Unmodulated *rf* field is commonly known as 'continuous wave' (CW) irradiation. CW irradiation has constant amplitude and has no phase modulation over time. CW has shorter bandwidth and hence not useful for large chemical shift differences. Theoretically it is possible to apply more power for higher chemical shift difference systems, but that may cause serious damage to *rf* probes.

(ii) Modulated lock can be realized by using CPD (composite pulse decoupling) pulses. As the name suggests, it is a phase modulated composite pulse, routinely used as a decoupling pulse sequence. In many cases it can outperform CW pulses as a spin-lock sequence. The bandwidth of CPD pulses are much larger compared to CW pulses and hence useful for larger chemical shift difference singlets. Commonly used CPD pulses are WALTZ-16, GARP etc.

During spin-lock the three triplet states' populations equilibrate rapidly under normal relaxation procedure, whereas singlet population being itself immune to *rf* spin-

lock, decays much slowly. After the fast decay of triplet states, singlet state achieve its maximum purity (singlet correlation may reach upto 0.997). Eventually singlet state also decays despite *rf* spin-lock shielding, but with much slower rate than any other states.

Now here we can recap the fact that singlet state itself is a zero quantum coherences and can not be directly accessible. Hence we must transfer the zero-quantum coherences to a observable single-quantum coherences to detect it. The following section describes the method in detail.

Singlet detection

The simplest method to detect singlet is to evolve it for a $1/(4\Delta\nu)$ chemical shift evolution and followed by a strong 90° pulse. The transformation of density matrix operator are as follows:

$$\begin{aligned} |S_0\rangle\langle S_0| = \quad & -\tfrac{1}{2}(I_+^1 I_-^2 + I_-^1 I_+^2) - I_z^1 I_z^2 + \tfrac{1}{4}\mathbb{1} \\ & \downarrow \tau_3 \\ & -\tfrac{1}{2i}(I_+^1 I_-^2 - I_-^1 I_+^2) - I_z^1 I_z^2 + \tfrac{1}{4}\mathbb{1}. \end{aligned}$$

This can also be written in terms of Cartesian product operator formalism:

$$-\tfrac{1}{2i}(I_+^1 I_-^2 - I_-^1 I_+^2) - I_z^1 I_z^2 + \tfrac{1}{4} = \tfrac{1}{2}(2I_x^1 I_y^2 + I_y^1 I_x^2) - I_z^1 I_z^2 + \tfrac{1}{4}.$$

Now a simple 90_0 pulse brings the magnetization into observable single quantum coherence.

$$\frac{1}{2}(2I_x^1 I_y^2 + I_y^1 I_x^2) - I_z^1 I_z^2 + \frac{1}{4}\mathbb{1} \xrightarrow{90_0} \frac{1}{2}(2I_x^1 I_z^2 - I_z^1 I_x^2) - I_y^1 I_y^2 + \frac{1}{4}\mathbb{1}. \tag{1.11}$$

These shows the antiphase transverse magnetization for the spin pair. The characteristic spectra for this kind of antiphase magnetization shows a typical “up-down-down-

up" pattern in the NMR peaks.

However one might notice that this way of detecting singlet states has less qualitative information. A better quantitative study can be carried out through tomographic method. In this context we have developed a robust density matrix tomographic technique which is particularly suitable for this problem. In the following section we will discuss the 'density matrix tomography' scheme in detail. Later we will apply this tomography sequence on singlets for its characterization in various experimental conditions.

1.3 Density Matrix Tomography

The delicate nature of 'quantum states' makes it vulnerable to macroscopic-world. The inevitable last step for most of the quantum information processing and quantum simulation is the measurement of derived quantum states. In the case of an ensemble quantum system, the states are presented by density matrix. In order to measure these density matrices, many sophisticated schemes have been envisaged. 'Density matrix tomography' technique has proven its utility for mapping any quantum states with high accuracy. It enables us to measure all the elements of a general density matrix at any time point. The knowledge of the full density matrix of any quantum state is important for many reason e.g. (i) one can find the error in the experiment, since we already have the knowledge about theoretical density matrix. (ii) Measuring density matrix at different time points of a dynamic quantum algorithm gives the pattern of population and coherence transfers. In the following section we have presented a robust tomographic scheme in the context of NMR [**?**].

Earlier schemes of tomography were designed in the context of quantum information processing [**?**, **?**]. They required spin-selective rotations and transition selective integrations of spectra. In homonuclear spin systems, particularly in ^{1}H spin systems, it is hard to design high fidelity spin-selective rotations owing to the small differences in chemical shifts (on the other hand, the heteronuclear singlet state is predicted to be short-lived [**?**]). These spin selective pulses generally tend to be long in duration, still in-

troduce significant errors. Integration of individual transitions is also problematic since the transitions, particularly those with mixed line shapes corresponding to a general density matrix, may severely overlap. Tomography based on two-dimensional NMR spectroscopy had also been proposed [**?**]. This is a general method in the sense only one 2D experiment is needed to be carried out irrespective of the size of the spin system. However, the 2D method is time consuming. Also since it relies on fitting the 2D cross-sections (along the indirect dimension) to mixed Lorentzian, the accuracy is limited by the quality of the fit that is achieved. In the following we present a robust density matrix tomography for a homonuclear weakly coupled two spins-1/2 system which needs only non-selective RF pulses and integrations over each spin instead of individual transitions [**?**].

The general traceless deviation density matrix consists of 15 independent real numbers:

$$\rho = \begin{pmatrix} p_0 & r_3 + is_3 & r_1 + is_1 & r_5 + is_5 \\ & p_1 & r_6 + is_6 & r_2 + is_2 \\ & & p_2 & r_4 + is_4 \\ & & & -\sum_{i=0}^{2} p_i \end{pmatrix}. \tag{1.12}$$

Here real elements p_k are populations and the complex elements $r_k + is_k$ correspond to single ($k = 1$ to 4), double ($k = 5$), and zero ($k = 6$) quantum coherences. The elements below the diagonal are determined by the Hermitian condition $\rho_{jk} = \rho_{kj}^*$. Since only single quantum coherences are directly observable, four combinations $R_1 := (r_1 + r_2)$, $S_1 := (s_1 + s_2)$, $R_2 := (r_3 + r_4)$, and $S_2 := (s_3 + s_4)$ can be obtained from the integration of complex line shapes of spins 1 and 2 respectively. Now consider an RF sequence with propagator U, that transforms the original density matrix ρ into $\rho' = U\rho U^\dagger$. Single quantum coherences of ρ' will lead to different linear combinations of various elements in ρ. Thus, by applying different propagators on ρ, we can measure the values of different linear combinations of various elements of ρ. The real and imaginary values of the

integration of jth spin in kth experiment will be labeled as R_j^k and S_j^k respectively. Following six one-dimensional NMR experiments were found to be sufficient to tomograph a two-spin density matrix:

1. $\mathbb{1}$
2. 90_x
3. $\frac{1}{4J} \cdot 180_x \cdot \frac{1}{4J}$
4. $45_x \frac{1}{4J} \cdot 180_x \cdot \frac{1}{4J}$
5. $45_y \frac{1}{4J} \cdot 180_x \cdot \frac{1}{4J}$
6. $\frac{1}{2\Delta\nu} \cdot 45_y \frac{1}{4J} \cdot 180_x \cdot \frac{1}{4J}$

Here $\mathbb{1}$ is the identity i.e., direct observation without applying any extra pulses. $\Delta\nu$ and J are the chemical shift difference and the scalar coupling respectively (both in Hz). The offset is assumed to be at the center of the two doublets and the RF amplitudes are assumed to be much stronger than $\Delta\nu$. By calculating the propagator for each of these experiments, 24 linear equations are achieved. Solving these equations, gives the all unknown parameters of the density matrix. A detailed analysis of the density matrix tomography scheme is given in Appendix A.

Now we will use this tomographic scheme on long-lived singlet states [**?**].

1.4 Singlet State Characterization

1.4.1 Observing through antiphase magnetization

The singlet state was prepared by the RF spin-lock method and converted into antiphase magnetizations as described by Carravetta and Levitt [**?**] using the pulse sequence shown in Figure 1.2a. The RF spin-lock was achieved by either CW irradiation

Figure 1.1: Part of the ^{1}H spectrum of 5-bromothiophene-2-carbaldehyde (inset), displaying the doublets corresponding to the two ^{1}H spins used to study the singlet state. The sample was dissolved in dimethyl sulphoxide-D6 and all the experiments are carried out at 300 K. The difference $\Delta\nu$ in chemical shifts is 192.04 Hz and the scalar coupling J is 4.02 Hz. Scalar coupling to aldehyde proton was too weak to be observed. The spin lattice relaxation time constants (T_1) for the two spins obtained from inversion recovery experiment are 5.2 s and 6.2 s respectively for the spins 1 and 2.

or by WALTZ-16 modulations. The RF offset was set to the center of the two chemical shifts in these experiments. The total magnitude of the antiphase magnetizations decays at different rates depending on the spin-lock conditions (Figures 1.3 and 1.4). The decay constants with CW spin-lock are 16.6 s (Figure 1.3a) and 13.4 s (Figure 1.3h) respectively at RF amplitudes of 2 kHz and 500 Hz. Under WALTZ-16 spin-lock, the decay constants are slightly smaller, 16.2 s (Figure 1.4a) and 12.8 s (Figure 1.4h) respectively at 2 kHz and 500 Hz. Nevertheless, these values are about 2 to 3 times the T_1 values of the individual spins implying the preparation of long-lived singlet state.

In this scheme, the integrated magnitude spectrum is usually monitored as a function of spin-lock time. The contributions from the spurious coherences may not be eliminated in this process. Further, the double quantum coherences, if any, are not observed at all. Our interest is to quantify the singlet content in the instantaneous state $\rho(t)$ during the spin-lock. One might guess that the singlet content is maximum in the beginning and exponentially decays with the spin-lock time. Further, one may also guess that CW spin-lock is superior to WALTZ-16 spin-lock at all timescales. But the following tomography results provide a different picture [**?**].

1.4.2 Tomography under varying spin-lock duration

The pulse sequence for the tomography of singlet states is shown in Figure 1.2b. The density matrix of the singlet state is $|S_0\rangle\langle S_0| = \frac{1}{4}\mathbb{1} + \rho_s$, with the traceless part $\rho_s = -I^1 \cdot I^2$ being the product of spin angular momentum operators of spins 1 and 2. The correlation

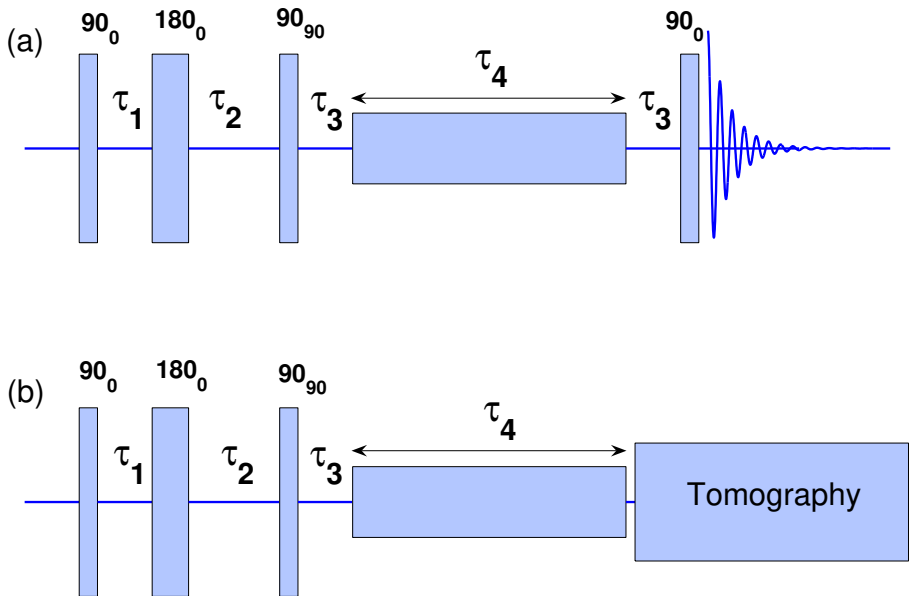

Figure 1.2: The pulse sequences for the preparation of singlet states and detection via (a) converting to antiphase single quantum magnetization and (b) tomography of singlet states. Here $\tau_1 = 1/(4J)$, $\tau_2 = 1/(4J) + 1/(2\Delta\nu)$, and $\tau_3 = 1/(4\Delta\nu)$, with $\Delta\nu$ and J being the chemical shift difference (in Hz) and the scalar coupling respectively. τ_4 is the duration of spin-lock.

of the theoretical singlet state operator ρ_s in the instantaneous experimental density matrix $\rho(t)$ (obtained from tomography),

$$\langle\rho_s\rangle(t) = \frac{\text{trace}\left[\rho(t)\cdot\rho_s\right]}{\sqrt{\text{trace}\left[\rho(t)^2\right]\cdot\text{trace}\left[\rho_s^2\right]}}, \tag{1.13}$$

gives a measure of singlet content in $\rho(t)$. The normalization used in the above expression disregards the attenuation of $\rho(t)$ itself. Similar definitions can be applied to calculate the correlations $\langle I_x^1\rangle$, $\langle|T_0\rangle\langle T_0|\rangle$, etc. We monitored the correlations as a function of spin-lock time τ_4 from 0 s to 30 s in steps of 0.5 s under different spin-lock conditions using the sequence shown in Figure 1.2b. The results are shown in Figures 1.3 and 1.4. 3D bar plots of full density matrices at two particular spin-lock conditions are shown in Figure 1.5.

The Figures 1.3b, 1.3i, 1.4b, and 1.4i indicate correlation $\langle\rho_s\rangle$ as a function of spin-

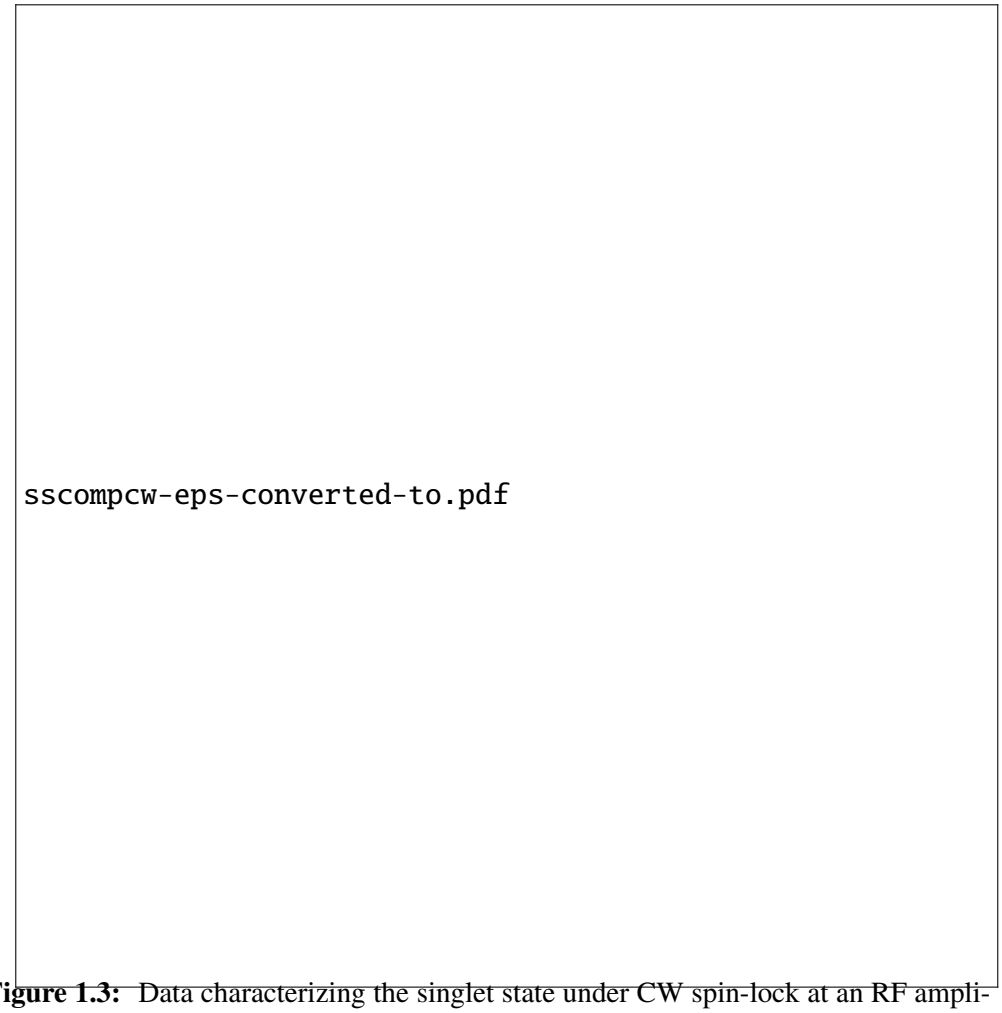

Figure 1.3: Data characterizing the singlet state under CW spin-lock at an RF amplitude of 2 kHz (a to g) and of 500 Hz (h to n). The spin-lock duration τ_4 was varied from 0 s to 30 s in steps of 0.5 s in each case. Dots in (a) and (h) correspond to the total magnitude of antiphase magnetization obtained from the pulse sequence in Figure 1.2a. Singlet decay constant T_s was obtained by using an exponential fit (smooth lines in (a) and (h)). During each fit, first two data points were omitted in view of strong spurious coherences created by the imperfections in the pulses. Remaining graphs are the results obtained from tomography using the pulse sequence shown in Figure 1.2b. They correspond to the correlations: $\langle \rho_s \rangle$ (b and i), $\langle I_x^p \rangle$ (c and j), $\langle I_y^p \rangle$ (d and k), $\langle I_z^p \rangle$ (e and l), $\langle I_+^1 I_+^2 + I_-^1 I_-^2 \rangle$ (f and m), and $c_q = \langle |T_q\rangle\langle T_q| \rangle$ (g and n), with spin numbers $p = \{1, 2\}$ and triplet subscripts $q = \{-1, 0, +1\}$.

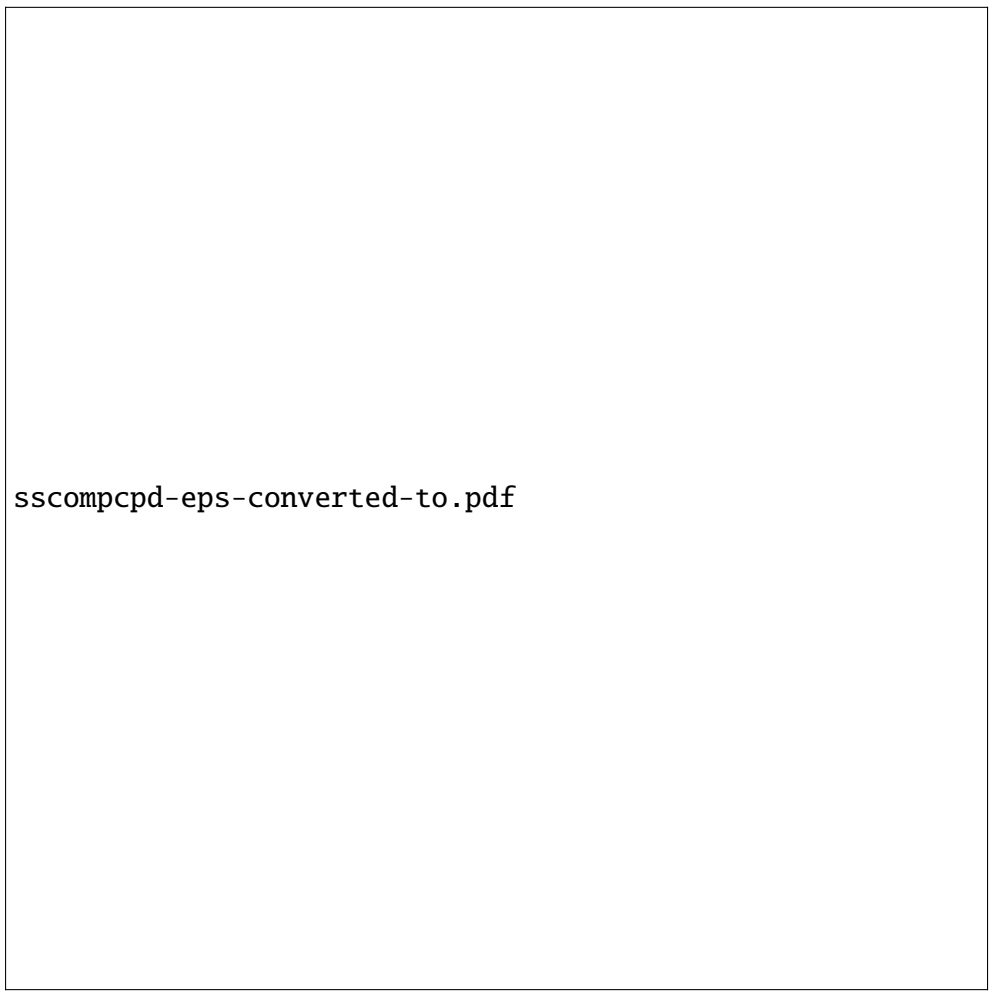

Figure 1.4: Similar data as in Figure 1.3, but under WALTZ-16 spin-lock at an RF amplitude of 2 kHz (a to g) and of 500 Hz (h to n). The graphs correspond to total magnitude of antiphase magnetization (a and h), $\langle \rho_s \rangle$ (b and i), $\langle I_x^p \rangle$ (c and j), $\langle I_y^p \rangle$ (d and k), $\langle I_z^p \rangle$ (e and l), $\langle I_+^1 I_+^2 + I_-^1 I_-^2 \rangle$ (f and m), and $c_q = \langle |T_q\rangle\langle T_q| \rangle$ (g and n), with spin numbers $p = \{1, 2\}$ and triplet subscripts $q = \{-1, 0, +1\}$.

lock time under various spin-lock conditions. In all the cases, the initial correlation is about 0.8. This is expected, since the initial state prepared by the pulse sequences in Figure 1.2 just before the spin-lock is actually

$$\rho(0) = |S_0\rangle\langle S_0| - |T_0\rangle\langle T_0|. \tag{1.14}$$

With CW spin-lock at a high RF amplitude of 2 kHz (Figure 1.3b - 1.3g), the singlet correlation $\langle\rho_s\rangle$ quickly reaches to 0.95 in 0.5 s of spin-lock time (Figure 1.3b). Most of the spurious coherences and the residual longitudinal magnetizations created during the preparation are destroyed by the RF inhomogeneity during spin-lock. Figures 1.3g and 1.3n reveal that the initial correlation $\langle|T_0\rangle\langle T_0|\rangle(0)$ is $-0.7 \sim 1/\sqrt{2}$ which is just expected . Within 0.5 s, the $|T_0\rangle\langle T_0|$ content is rapidly reduced. But complete equilibration of triplet levels takes about 5 s. Interestingly, there is a sudden build-up and gradual fall of double quantum coherence as seen in Figures 1.3f and Figures 1.3m. As the singlet state gets purified, $\langle\rho_s\rangle$ exceeds 0.99 in 6 seconds and reaches a maximum value of 0.994 at 9.5 s. After about 18 s, $\langle\rho_s\rangle$ starts decaying below 0.99, probably due to the gradual conversion of singlet state to other magnetization modes via the triplet states by relaxation mechanisms. On the other hand, there is a gradual build up of y- and z-magnetizations (Figures 1.3d and 1.3e) in a similar way as that of a steady state experiment [**?**, **?**]. Nevertheless, the singlet correlation remained above 0.95 till 30 s. The x-magnetization and the double quantum coherence (Figures 1.3c and 1.3f) remained small during the period of high correlation. After the initial differences, the triplet states equilibrate in about 6s, and remain steady then onwards (Figures 1.3g and 1.3n).

With CW spin-lock at 500 Hz , the singlet correlation reaches only up to 0.94 again at about 9 s and then steadily drops to 0.71 at 30 s (Figure 1.3i). The increased buildup of x-, y-, and z- magnetizations with the reduction of the spin-lock power can also be noticed (Figure 1.3j - 1.3l).

Under WALTZ-16 spin-lock (Figure 1.4), all the graphs are characterized by oscillations that are either in-phase or anti-phase. The origin of oscillations probably lies in

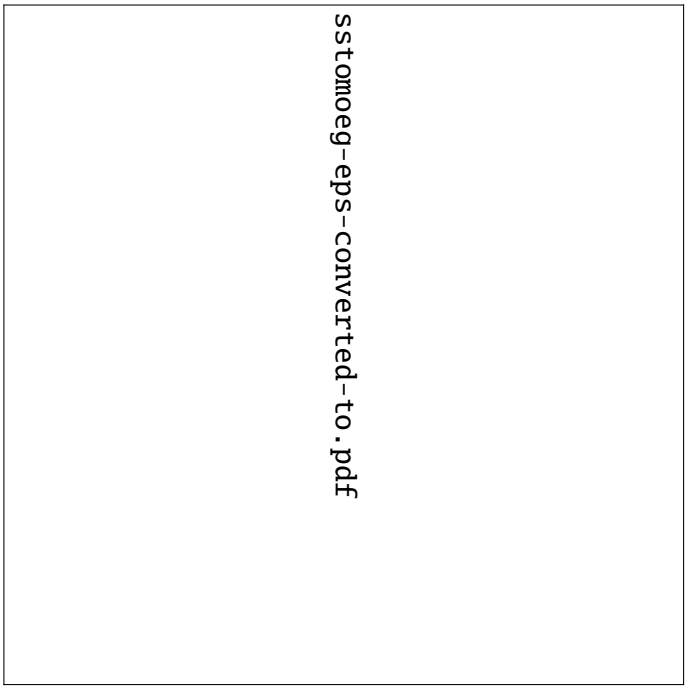

Figure 1.5: Bar plots showing (a) traceless part ρ_s of the theoretical singlet state density matrix, (b) experimental state after 15 s of WALTZ-16 spin-lock at an RF amplitude of 2 kHz, and (c) experimental state after 14 s of WALTZ-16 spin-lock at an RF amplitude of 500 Hz. The upper and lower traces correspond to the real and imaginary parts respectively. The singlet correlations in (b) and (c) are respectively 0.997 and 0.547. The density matrix in (b) shows significant decay, but still has high singlet content! The real part of the density matrix in (c) shows significant double quantum artifact.

the cyclic nature of WALTZ-16 modulation.

At an RF amplitude of 2 kHz, the maximum singlet correlation of 0.997 was reached at 15 s(Figure 1.4b). The 3D bar plot of the density matrix corresponding to this case is shown in Figure 1.5b. More interestingly, $\langle\rho_s\rangle$ peaks seem to maintain above 0.99 till $\tau_4 = 28.5$ s, i.e., about 10 s longer than the CW case! Thus, for certain values of spin-lock durations, WALTZ-16 provides purer singlet states than that of CW.

The singlet correlation under WALTZ-16 spin-lock at 500 Hz displays stronger oscillations (Figure 1.4i). Despite the oscillations, the singlet correlation reaches as high as 0.96 at 13.5 s. Again it can be noticed that good singlet content is held for longer periods by WALTZ-16 than the CW of same amplitude. For example at 500 Hz RF

amplitude, WALTZ-16 gives a singlet correlation of 0.94 at τ_4 = 27 s, while that for CW it is only 0.79.

1.4.3 Offset dependence

Theoretical and numerical investigations on the offset dependence of singlet spin-lock has been have been carried out by Karthik and Bodenhausen [**?**] and by Pileio and Levitt [**?**]. Robustness of various modulation schemes with regard to offset of singlet spin-lock have been demonstrated by Bodenhausen and co-workers [**?**]. Here we probe the offset dependence of singlet evolution using tomography [**?**]. Figure 1.6 shows the experimental data obtained from a series of singlet state tomography experiments, each time varying the RF offset of the spin-lock. The RF offset was measured from the center of the two chemical shifts. Again the experiments were carried out under the following spin-lock conditions:

(i) CW for 15s (Figure 1.6a-1.6f),

(ii) CW for 28.5s (Figure 1.6g-1.6l),

(iii) WALTZ-16 for 15s (Figure 1.6m-1.6r), and

(iv) WALTZ-16 for 28.5s (Figure 1.6s-1.6x).

The graphs indicate that the WALTZ-16 scheme is far superior compared to CW in preserving the singlet correlation at high RF offsets. The singlet correlations with 2 kHz CW drops below 0.5 for an offset of 50 Hz. However, WALTZ-16 at 2 kHz amplitude maintains a high correlation of 0.97 at 28.5s, even with an offset of 2.1 kHz. In the case of CW spin-lock, rapid build up of y-magnetizations can be noticed with the increase of the RF offset [**?**].

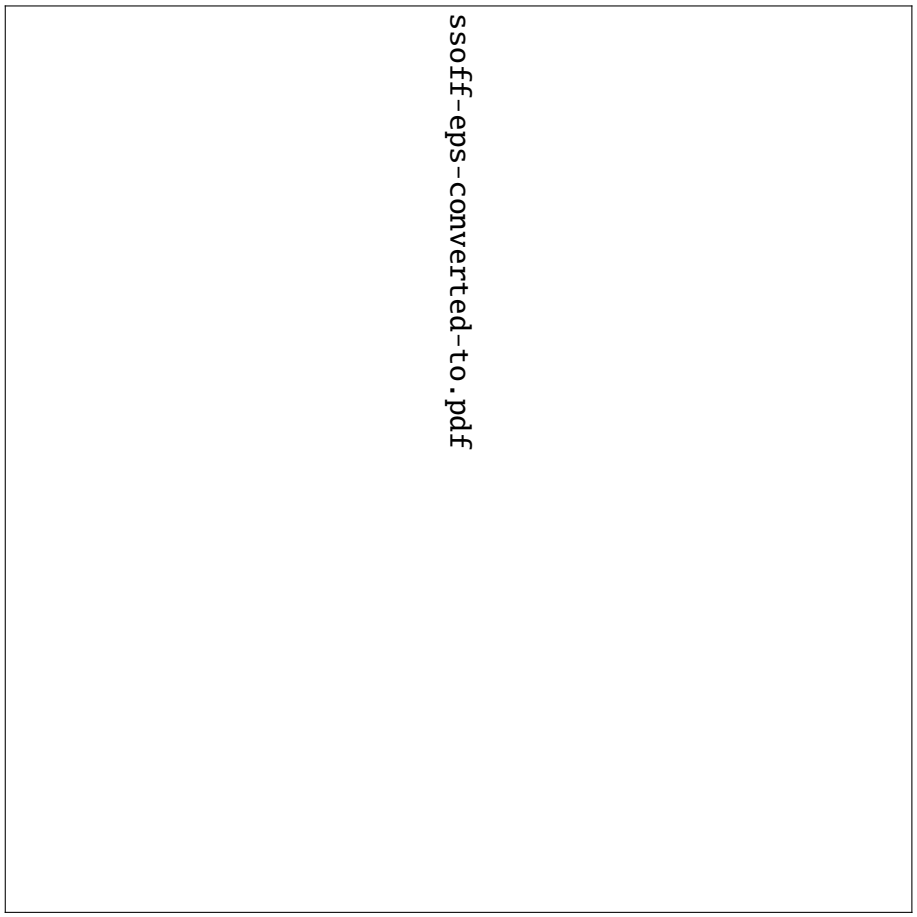

Figure 1.6: Correlations calculated using the density matrix tomography of singlet states prepared with different spin-lock conditions: (i) CW spin-lock at 2 kHz for 15s (a to f), (ii) CW spin-lock at 2 kHz for 28.5s (g to l), (iii) WALTZ-16 spin-lock at 2 kHz for 15s (m to r), and, (iv) WALTZ-16 spin-lock at 2 kHz for 28.5s (s to x). In each case, the horizontal axis indicates the RF offset $\Delta\nu$ during the spin-lock. The offset is measured from the center of the two chemical shifts. The rows correspond to : $\langle\rho_s\rangle$ (b and i), $\langle I_x^p\rangle$ (c and j), $\langle I_y^p\rangle$ (d and k), $\langle I_z^p\rangle$ (e and l), $\langle I_+^1 I_+^2 + I_-^1 I_-^2\rangle$ (f and m), and $c_q = \langle|T_q\rangle\langle T_q|\rangle$ (g and n), where spin numbers $p = \{1$ (pluses), 2 (×'s)$\}$ and triplet subscripts $q = \{-1$ (dots), 0 (circles), +1 (pluses)

.

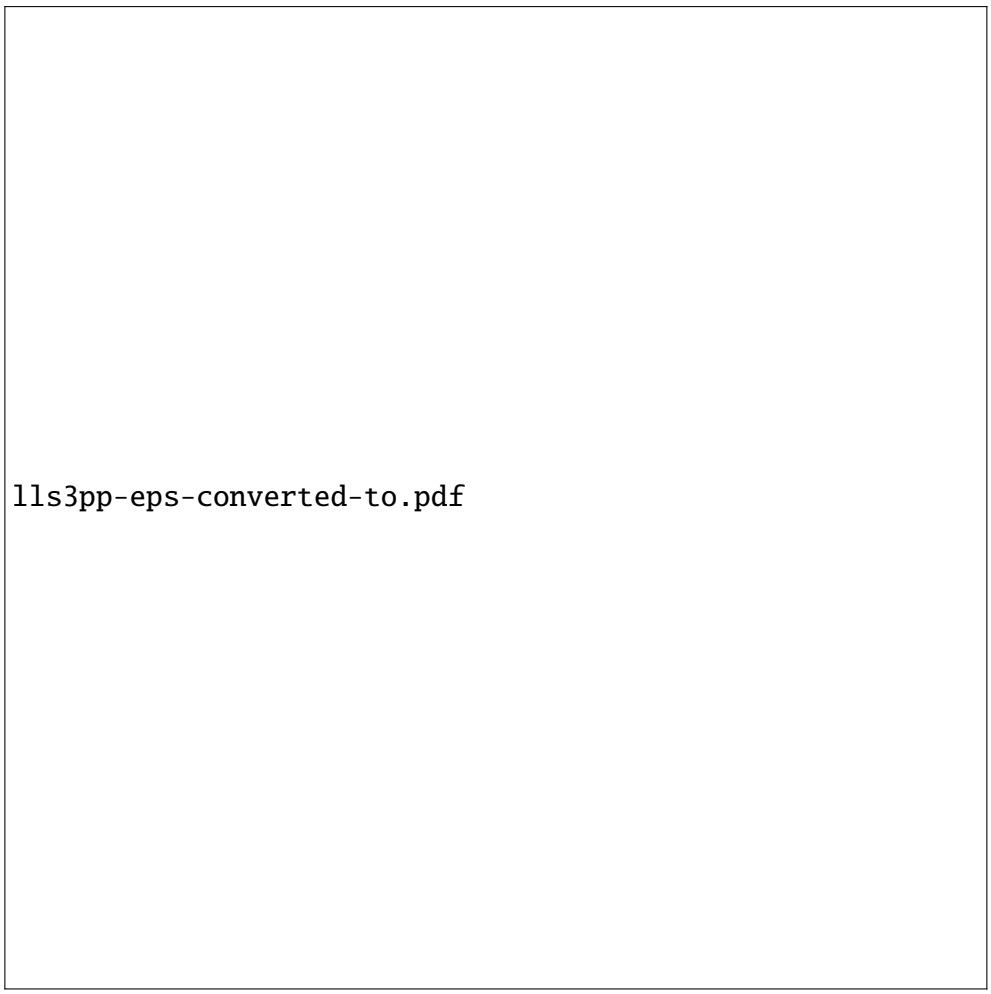

Figure 1.7: Pulse sequence for the creation of long lived singlet states in a 3 spin system (AMX). (a) Anti-phase singlet magnetization to be accessed via spin-3, (b) qualitative measure of singlet correlation is done by state tomography. τ_1 and τ_2 are optimized delays in a way that both J_{13}, J_{23} get a $\pi/2$ J- evolution, $\tau_3 = \frac{1}{4\Delta\nu_{12}}$, and τ_4 is the spin-lock duration.

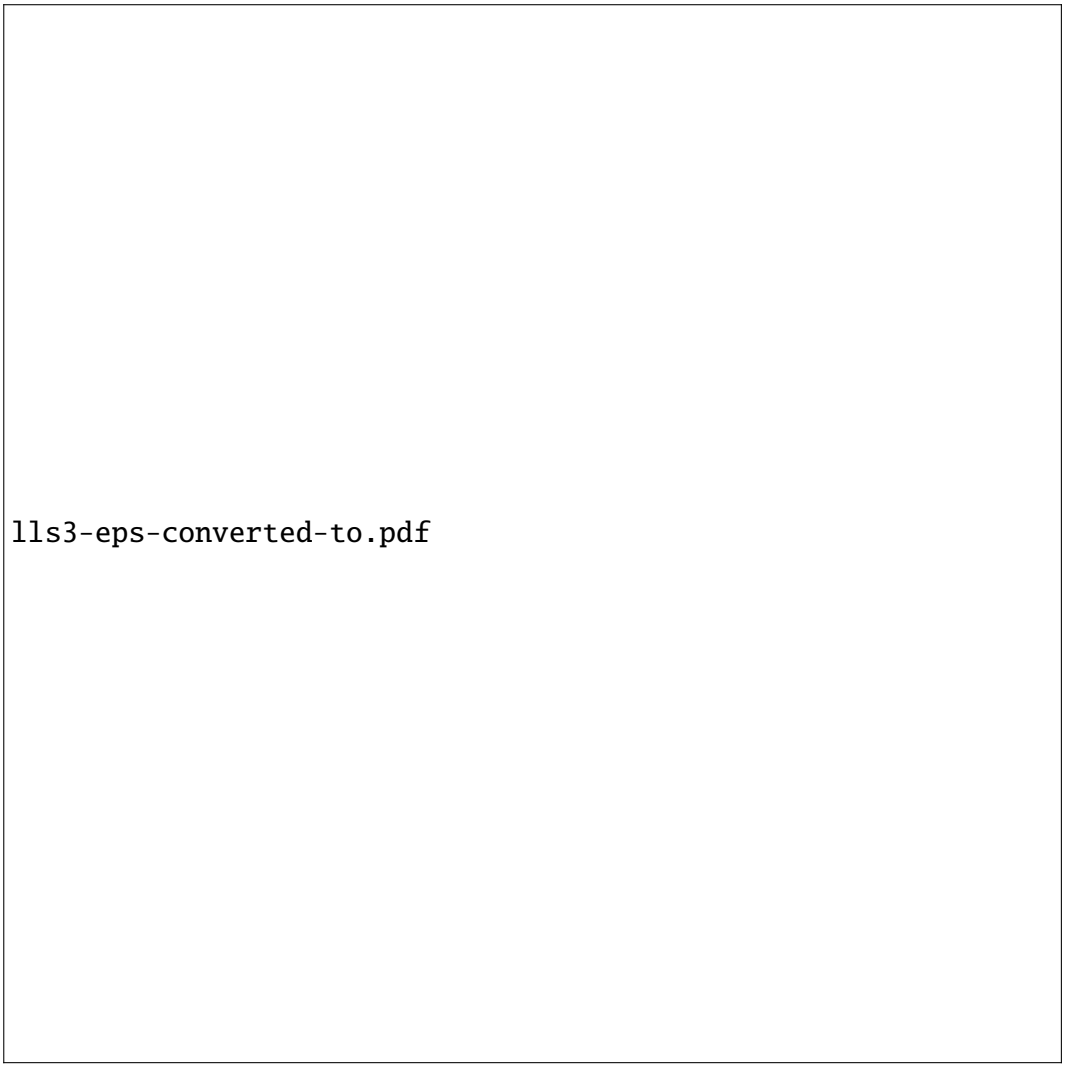

Figure 1.8: Experimental results of 3-spin LLS. (a) Acrylonitrile dissolved in $CDCl_3$, where 3 protons acting as a three spin homonuclear system. (b) The ^1H reference spectra of Acrylonitrile in a 500 MHz spectrometer. (c) and (d) showing the antiphase spectra of spin-3 after a spin lock duration of 5 s and 40 s respectively. (e) The solid curve showing the antiphase magnetization decay and dotted curve showing the singlet correlations obtained from tomography over a duration of spin-lock (τ_4) time.

1.5 Long lived singlet states in multi-spin systems

1.5.1 Long lived singlet states in a 3-spin system

In this subsection we will describe the methods for preparing long lived singlet states in a 3-spin system (AMX). We have extended the procedure of the 2-spin system as described in the previous sections. The singlet population distribution between any two spins can be prepared in presence of a third spin. The pulse sequence relies on the refocusing of the unnecessary couplings. The NMR pulse sequence is shown in Fig. 1.7. In this particular example we have prepared the singlet population between spin-1 and spin-2. Singlet population is accessed by transferring the magnetization into spin-3 . The quantitative measure of singlet magnetization is done by the pulse sequence shown in Fig. 1.7a. The extensive tomographic method of accessing singlet correlation has also been performed. The experimental results are shown in Fig. 1.8. The decay of antiphase magnetization and tomographic correlation is shown in Fig. 1.8e. The T_1 time for all the three spins are roughly 6 sec, while the LLS time (T_{LLS}) is found to be 17.9 sec. Hence the ratio $T_{LLS}/T_1 \approx 3$. The nature of this plot is similar to the spin-2 system and the reason for this is given in previous section. The 3-spin density matrix tomography scheme is described in detail in Appendix B.

1.5.2 Long lived singlet states in a 4-spin system

We have prepared two pair of singlet states in a 4 spin $AMXY$ system. The exact pulse sequence is shown in Fig. 1.9. We were able to prepare simultaneous singlet states in between spin-1 and spin-2 and also in between spin-3 and spin-4. The J-evolution delays (τ_1 and τ_2) are calculated in a optimized way. The traditional method of accessing singlet states is by converting it into single quantum coherences. The antiphase spectra of aspirin are shown in Fig. 1.10c. We have done density matrix tomography to calculate the correlation at various spin-lock duration. The nature of antiphase decay and singlet correlation profile matches with the previous cases (2-spin and 3-spin) and hence got the

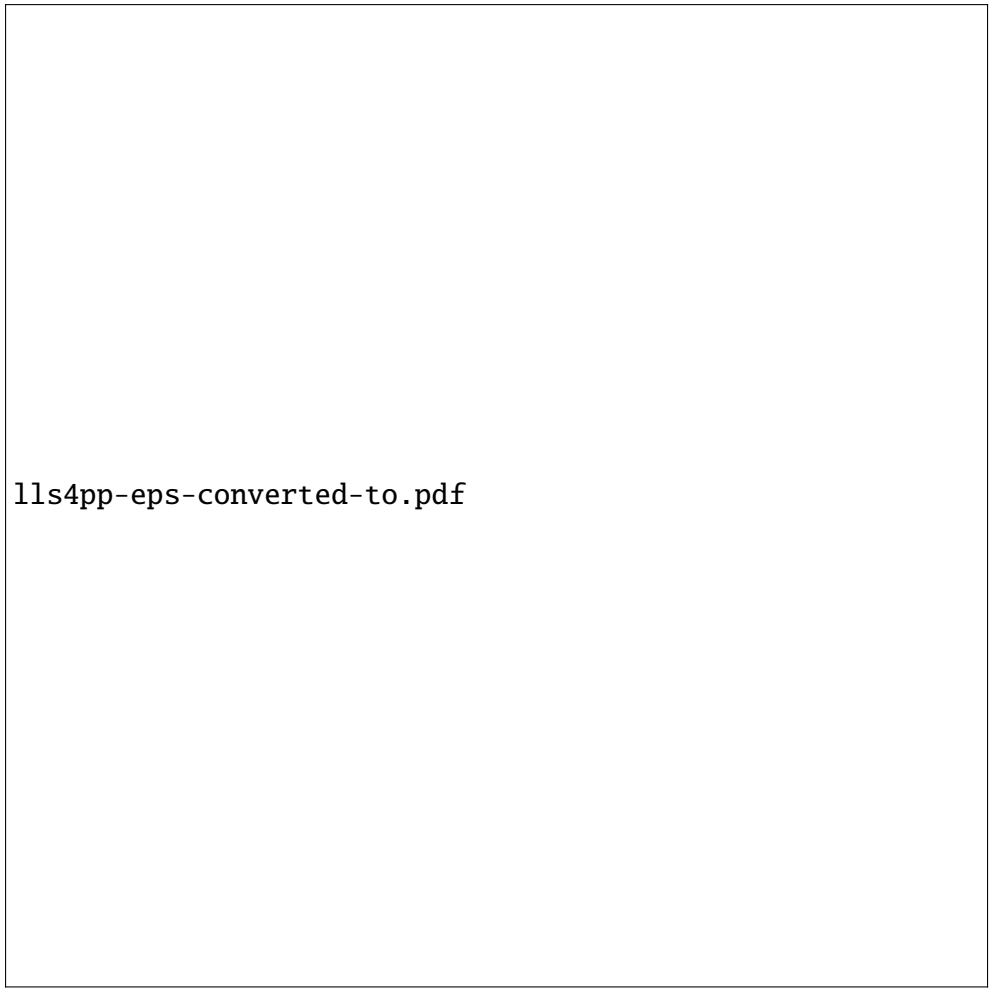

Figure 1.9: Pulse sequence for the creation of long lived singlet states in a 4 spin system ($AMXY$). (a) Singlet states accessed by transferring it into anti-phase magnetization, (b) qualitative measure of singlet correlation is done by state tomography. τ_1, τ_2 are optimized delays and τ_4 is the spin-lock duration. 90_{ph} denoting a optimized phase $\pi/2$ non-selective pulse.

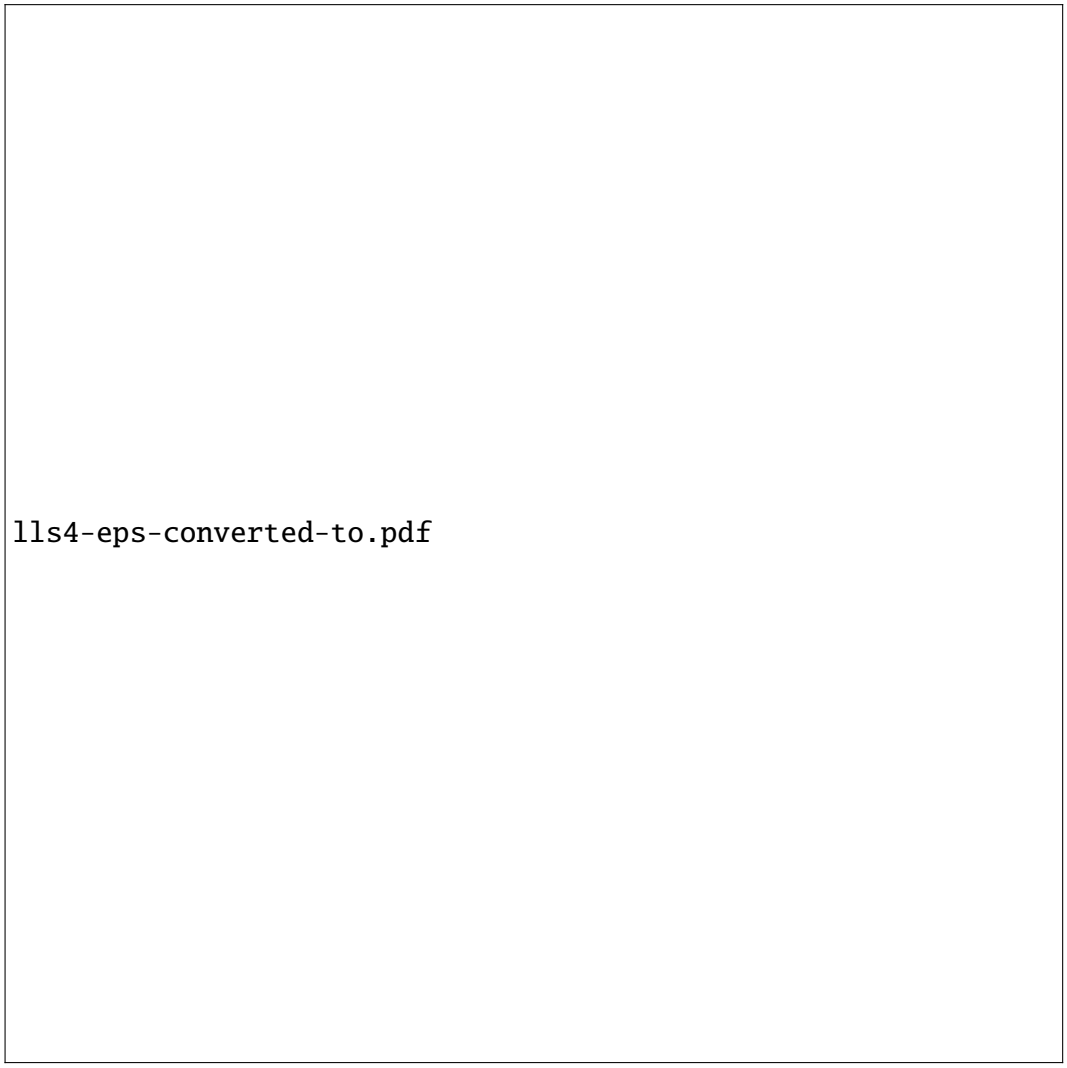

Figure 1.10: Experimental results of 4-spin LLS. (a) Aspirin dissolved in CD_3OD, where 4 protons acting as a four spin homonuclear system. (b) The chemical shifts and J-coupling constants in Hz are shown in a table format. (c) The ^1H reference spectra of Aspirin is at the bottom trace. The antiphase spectra are shown in upper trace after a spin lock duration of 3 s and 10 s respectively. (d) The solid curve showing the antiphase magnetization decay and dotted curve showing the 1-2 singlet correlations obtained from tomography over a duration of spin-lock (τ_4) time.

similar explanation. We have found $T_1 \approx 3s$ and $T_{LLS} \approx 6s$, hence the ratio $T_{LLS}/T_1 \approx 2$. This also proves the long lived nature of the prepared singlet states.

1.6 Conclusions

Study of singlet state is important not only because of the interesting Physics that makes it long-lived, but also because of its potential for a number of applications. We have studied the singlet state directly and quantitatively using density matrix tomography. A new set of tomography sequences have been introduced for this purpose. The density matrix tomography provides a tool not only for characterizing various spin-lock schemes but also for understanding the spin dynamics during the spin-lock period.

The singlet state is preserved with CW spin-lock as well as with WALTZ-16 spin-lock at two different RF amplitudes: 2 kHz and 500 Hz. The results indicate that at high RF amplitudes, both CW and WALTZ-16 achieve high singlet content. An important feature of singlet state is that it gets purified by itself during the spin-lock, simply because of its longer life time compared to the spurious coherences. There exist optimum spin-lock values at which the singlet correlations are maximum. While WALTZ-16 shows significant oscillations in the singlet purity, for certain intervals of spin-lock it gives better performance than CW and holds the singlet content for longer intervals of time. The dependence of correlations with the RF offset during the spin-lock are also studied under both CW and WALTZ-16 schemes. It is found that WALTZ-16 is far superior in preserving the singlet state at large RF offsets.

Chapter 2

Storing Entanglement Via Dynamical Decoupling

In this chapter, we have described the experimental study of dynamical decouplings in preserving two-qubit entangled states using an ensemble of spin-1/2 nuclear pairs in solution state. A brief introduction of decoherence and dynamical decouplings are given in section 4.1. In section 4.2, we have described Uhrig's dynamical decoupling and its usefulness in preserving coherence orders. In section 4.3, we have shown the creation of Bell states from long-lived singlet state. In section 4.4, experimental results are shown for storing coherence orders in Bell states including singlet state. We found that the performance of odd-order Uhrig sequences in preserving entanglement is superior to both even-order Uhrig sequences and periodic spin-flip sequences. We also found that there exists an optimal order of the Uhrig sequence using which the singlet state can be stored at high correlation for about 30 seconds.

2.1 Introduction

Harnessing the quantum properties of physical systems have several potential applications, particularly in information processing, secure data communications, and quantum

simulators [**?**]. It is believed that such quantum devices may play an important role in future technology [**?**]. But their physical realization is challenging mainly because of decoherence - the decay of the coherent states due to interaction with the surrounding environment [**?**, **?**]. Therefore it is important to minimize the effects of decoherence using suitable perturbation on the quantum system [**?**]. A technique, known as 'dynamical decoupling' involves protecting the quantum states from decoherence by driving the system in a systematic manner such that the effective interactions with the environment at different instants of time cancel one another.

In the following subsections we will describe the effect of decoherence and saving coherence through dynamical decouplings.

2.1.1 Decoherence

As the name suggests, decoherence means loss of coherence order in a system which comprises with more than one entities. The idea of decoherence in quantum mechanics came much earlier in 1952 [**?**] in the context of hidden variable model. It was first developed due to the possible explanation of the appearance of wave function collapse [**?**, **?**]. Decoherence based explanation started getting acceptance in early 1980 [**?**, **?**]. However, Decoherence became inevitable tool of understanding quantum mechanical interactions in the context of quantum information processing later. Soon it became clear that, decoherence is one of the biggest challenges to be overcome in order to realize a practical quantum computer.

Let us consider an isolated 2-level quantum system (a single spin-1/2 system). The wave function can be represented by following :

$$|\psi\rangle = c_0|0\rangle + c_1|1\rangle, \tag{2.1}$$
$$\text{with,} \qquad |c_0|^2 + |c_1|^2 = 1.$$

The system can be best represented by the density matrix formalism :

$$\begin{aligned}\rho_s &= |\psi\rangle\langle\psi| \\ &= c_0c_0^*|0\rangle\langle 0| + c_1c_1^*|1\rangle\langle 1| + c_0c_1^*|0\rangle\langle 1| + c_1c_0^*|1\rangle\langle 0|,\end{aligned}$$

$$= \begin{array}{c} \\ \langle 0| \\ \langle 1| \end{array} \begin{array}{c} \begin{array}{cc} |0\rangle & |1\rangle \end{array} \\ \begin{pmatrix} c_0c_0^* & c_0c_1^* \\ c_1c_0^* & c_1c_1^* \end{pmatrix} \end{array} \tag{2.2}$$

The diagonal elements are representing the population distribution of the system in two states. The off-diagonal elements are the coherence terms. Here, we are interested in the evolution of the coherence terms once the system is no more an isolated quantum system and is interacting with the environment. The interaction of system-environment is a non-unitary process and hence irreversible. Below we see the effect of environment on the 2-level super-positioned state.

$$|\psi\rangle|E\rangle = (c_0|0\rangle + c_1|1\rangle)|E\rangle \xrightarrow{U(\tau)} (c_0|0\rangle|E_0\rangle + c_1|1\rangle|E_1\rangle). \tag{2.3}$$

Now it can be noticed that the output state is an entangled state and can not be written as system and environment separately (unless $|E_0\rangle = e^{i\phi}|E_1\rangle$). In terms of density matrix, the situation can be represented as below :

$$\begin{aligned}\rho_s &= |\psi\rangle|E\rangle\langle\psi|\langle E| \\ &= c_0c_0^*|0\rangle\langle 0| \otimes |E_0\rangle\langle E_0| + c_1c_1^*|1\rangle\langle 1| \otimes |E_1\rangle\langle E_1| \\ &\quad + c_0c_1^*|0\rangle\langle 1| \otimes |E_0\rangle\langle E_1| + c_1c_0^*|1\rangle\langle 0| \otimes |E_1\rangle\langle E_0|.\end{aligned} \tag{2.4}$$

Now tracing out the environment from the system gives the necessary information about

the system and can be written as :

$$\begin{aligned}\rho_s &= \text{trace}_E[\rho_{SE}] \\ &= c_0c_0^*|0\rangle\langle 0| + c_1c_1^*|1\rangle\langle 1| + \langle E_1|E_0\rangle c_0c_1^*|0\rangle\langle 1| + \langle E_0|E_1\rangle c_1c_0^*|1\rangle\langle 0| \\ &= \begin{array}{c} \\ \langle 0| \\ \langle 1| \end{array} \begin{array}{c} \begin{array}{cc} |0\rangle & |1\rangle \end{array} \\ \begin{pmatrix} |c_0|^2 & \langle E_1|E_0\rangle c_0c_1^* \\ \langle E_0|E_1\rangle c_1c_0^* & |c_1|^2 \end{pmatrix} \end{array}. \end{aligned} \tag{2.5}$$

The above equation shows that the coherence terms obtains extra coefficients. Usually, when the environment has a large degree of freedom, these coefficients decay exponentially with time:

$$|\langle E_1(t)|E_0(t)\rangle| = e^{-\Lambda(t)}. \tag{2.6}$$

Hence, after a certain time duration, the coherence terms decay to zero.

2.1.2 Dynamical decoupling

Dynamical decoupling is a technique by which it is possible to suppress, at least to some extent, the environmental effect on a open quantum system under study. The idea of dynamical decoupling has connections to the routinely used NMR decoupling sequences where unwanted couplings are averaged out with the applications of suitable modulated or unmodulated RF pulse sequences. The dynamical decoupling scheme relies on the application of π pulses at certain intervals. Preserving nuclear spin coherences by spin flips at regular intervals was long been known in NMR as the famous Carr-Purcell-Meiboom-Gill (CPMG) sequence [**?**, **?**]. The CPMG sequence is widely used in NMR to measure the transverse relaxation time constants in the presence of spatial inhomogeneity of the static magnetic field and temporal fluctuations in the local fields arising due to the molecular motion [**?**]. The sequence involves a set of N number of π pulses uniformly distributed in a duration $[0, T]$ at time instants $\{t_1, t_2, \cdots, t_N\}$. Assuming in-

stantaneous π pulses, j^{th} time instant is linear in j,

$$t_j^{\text{CPMG}} = T\left(\frac{2j-1}{2N}\right). \tag{2.7}$$

Of course, in practice the π pulses do have finite duration owing to the limited power of electromagnetic irradiation generated by a given hardware. Further, the constant time period between these spin flips should ideally be shorter than the correlation time of the spin-bath interaction. Even, this delay is limited by the maximum duty-cycle that is allowed for the hardware. Dynamical decoupling with such bounded controls have also been suggested [**?**, **?**, **?**, **?**]. For instance Hao et al. have been able to calculate, using a particular type of atomic systems, the maximum delay between spin-flips in order to efficiently suppress decoherence due to a bath with a finite cut-off frequency [**?**]. By studying the efficiency of the decoupling as a function of the CPMG period often it is possible to extract valuable informations about molecular dynamics and such studies are broadly categorized under 'CPMG dispersion' experiments [**?**].

Recently in 2007, Uhrig generalized the CPMG sequence by considering an optimal distribution $\{t_1, t_2, \cdots, t_N\}$ of N spin flips in a given duration $[0, T]$ of time that provides most efficient dynamical decoupling [**?**]. Using a simple dephasing model, Uhrig proved that the time instants should vary as a squared sine bell:

$$t_j = T\sin^2\left(\frac{\pi j}{2N+2}\right). \tag{2.8}$$

UDD works well in systems having a high-frequency dominated bath with a sharp cutoff [**?**, **?**, **?**]. On the other hand, when the spectral density of the bath has a soft cutoff (such as a broad Gaussian or Lorentzian), the CPMG sequence was found to outperform the UDD sequence [**?**, **?**, **?**, **?**, **?**, **?**, **?**]. Suter and co-workers have studied these different regimes and arrived at optimal conditions for the dynamical decoupling [**?**].

Recently Agarwal has shown using theoretical and numerical calculations that even entangled states of two-spin systems can be stored more efficiently using UDD [**?**].

Since entangled states play a central role in QIP, teleportation, data encryption, and so on, saving entanglement is crucial for the efficient physical realization of quantum devices [**?**]. More recently dynamical decoupling on an electron-nuclear spin-pair in a solid state system has been shown to prolong the pseudoentanglement lifetime by two orders of magnitude [**?**].

While much of the experimental efforts have been on testing the loss of coherence due to T_2 processes, here in this chapter, we presented the first experiments where we study not only the loss of coherences, but also the loss of entanglement due to both T_1 and T_2 processes. Though newer sequences have been suggested to decouple both of these processes, these are yet to be studied experimentally [**?**, **?**]. We have developed experimental techniques where we can prepare Bell states with high fidelity and characterize these states with high precision [**?**, **?**]. we explore the utility of different dynamical decoupling sequences on systems wherein both T_1 and T_2 relaxations are significant.

2.2 Uhrig dynamical decoupling

Uhrig dynamical decoupling (UDD) claims to be more efficient than the CPMG sequence (which serves as the best known decoupling sequence for more than 50 years!) in preserving coherence orders. The efficiency of UDD over CPMG can be understood by various mathematical approaches. Uhrig [**?**] explained the efficiency of UDD by considering the standard spin-boson model in ohmic bath. This model predicts the noise-spectrum with a sharp cut-off. Here we describe the 'filter function analysis' in brief for the study of UDD's efficiency [**?**].

2.2.1 Efficiency of UDD over CPMG

We can write the Hamiltonian of a system interacting with an environment as[**?**, **?**],

$$\mathcal{H} = \frac{\hbar}{2}\left[\Omega + \beta(t)\right]\hat{\sigma}_z \tag{2.9}$$

where Ω is the unperturbed part representing the system and $\beta(t)$ is the time dependent fluctuating part due to environmental interaction. As in ref [**?**], the time evolution of a superposition state initially oriented along $\hat{Y}$ under the affect of this Hamiltonian can be written as

$$|\psi(t) = \frac{1}{\sqrt{2}}\left(e^{-i\Omega t/2}e^{-\frac{1}{2}\int_0^t \beta(t')dt'}|0\rangle + e^{i\Omega t/2}e^{\frac{1}{2}\int_0^t \beta(t')dt'}|1\rangle\right) \tag{2.10}$$

where $|0\rangle$ and $|1\rangle$ representing the basis states and $\beta(t')$ adding the random phase errors. Accumulation of such phases lead towards decoherence. A fundamental technique for preserving coherence in NMR is 'Spin-echo' given by Hahn [**?**]. Spin-echo works as a refocusing technique by applying a π pulse in between two exact delays. Hahn echo became indispensable tool for coherence reorder and soon it was realized that the application of series of π pulses at regular interval would be most effective in order to reduce dephasing [**?**, **?**]. Hahn echo acts as a high pass filter for an arbitrary noise spectrum $S_\beta(\omega)$ and it neutralize the phase errors by slowly Fourier components of β. Now this one π pulse logic can be extended to multiple π pulses technique as well. Application of multiple pulses on a qubit system, leads to coherence state as,

$$\begin{aligned} W(\tau) &= \left|\overline{\langle\sigma_Y\rangle(\tau')}\right| = e^{-\chi(\tau)}, \\ \text{where,} \qquad \chi &= \frac{2}{\pi}\int_0^\infty \frac{S_\beta(\omega)}{\omega^2}F(\omega t)d\omega. \end{aligned} \tag{2.11}$$

Here, the filter function $F(\omega\tau)$ contains all the necessary information regarding the efficiency of pulse sequence for preserving coherence against the environment influence

$S_\beta(\tau)$. Now, $F(\omega\tau)$ can be calculated from

$$F(\omega\tau) = |\tilde{y}_n(\omega\tau)|^2 , \tag{2.12}$$

where $|\tilde{y}_n(\omega\tau)|$ is the Fourier transform of time domain filter function $y_n(t)$. Any modification of filter function will give different efficiency power of that particular pulse sequence. CPMG sequence having π pulses at regular interval was modified by Uhrig by repositioning the π pulses at irregular intervals. Noise reduction is shown to be much more efficient for Uhrig sequence than CPMG [**?**, **?**].

Later, Agarwal has shown that this results of efficient UDD can be generalized for an entangled system as well [**?**]. Here our work mainly focuses on the experimental studies of UDD and CPMG on such an entangled states as well as on non-entangled states.

2.3 Preparation of Entanglement

We study storage of entanglement by dynamic decoupling on a pair of spin-1/2 nuclei using liquid state NMR techniques. The sample consisted of 5 mg of 5-chlorothiophene-2-carbonitrile dissolved in 0.75 ml of dimethyl sulphoxide (see Figure 2.1). The two protons of the solute molecule differ in the Larmor frequency by $\Delta\nu = 270.4$ Hz and have an indirect spin-spin coupling constant of $J = 4.1$ Hz. The T_2 relaxation time constants for the two protons are about 2.3 s and the T_1 relaxation time constants are about 6.3 s.

2.3.1 Preparation of singlet states

High fidelity entangled states are prepared via long lived singlet states in a procedure described in chapter 2.

The long-lived nature of singlet states under the equivalence Hamiltonian can be used to prepare high-fidelity Bell states. The experiment involves preparing an incoher-

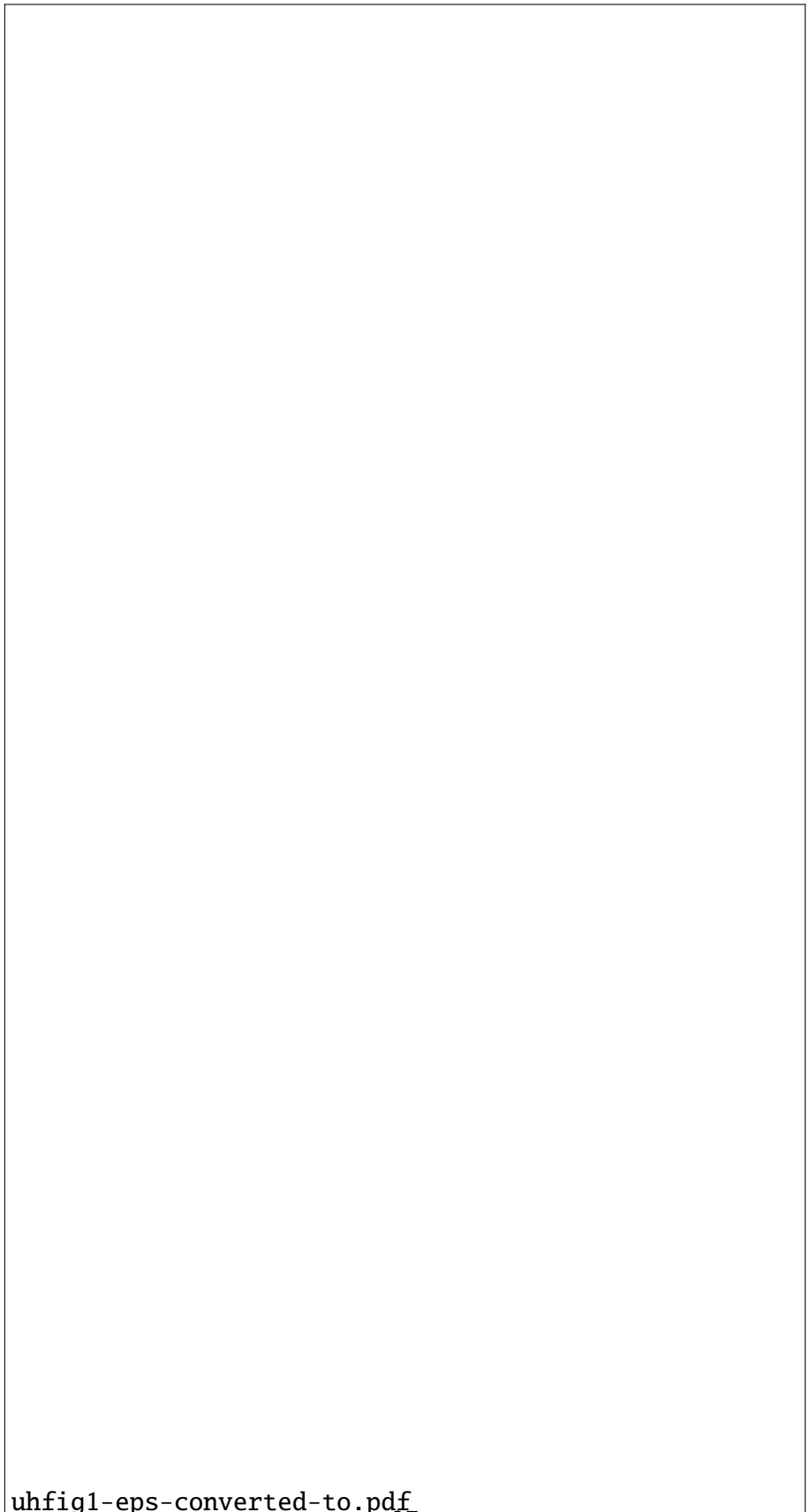
uhfig1-eps-converted-to.pdf

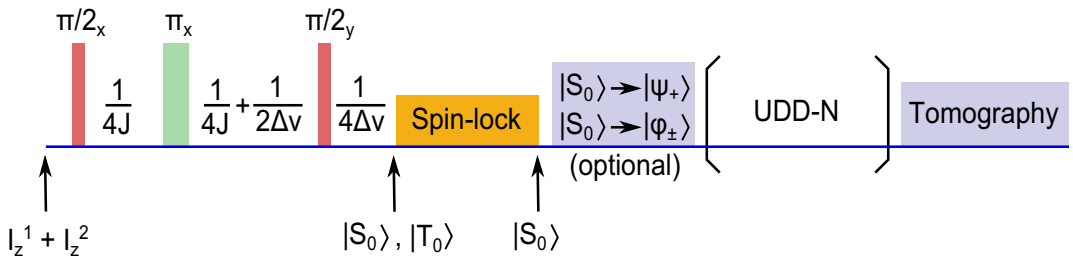

Figure 2.2: NMR pulse sequence to study dynamical decoupling on Bell states. An incoherent mixture of singlet and triplet states is prepared which under spin-lock purifies to singlet state. The resulting singlet state can be converted to other Bell states. Then dynamical decoupling sequence can be applied and the performance of the sequence can be studied by characterizing the residual state using density matrix tomography.

ent mixture of singlet and triplet states,

$$\rho(0) = -\boldsymbol{I}^1 \cdot \boldsymbol{I}^2 \equiv |S_0\rangle\langle S_0| - |T_0\rangle\langle T_0| \tag{2.13}$$

from the equilibrium state $I_z^1 + I_z^2$ by using the pulse sequence shown in Figure 2.2 [**?**]. During the spin-lock $|T_0\rangle$ state rapidly equilibrates with the other triplet states. On the other hand, the decay constant of singlet state $|S_0\rangle$ during the spin-lock is much longer than the spin-lattice relaxation time constant (T_1) (and hence the singlet state is known as a long-lived state) [**?**, **?**]. Hence at the end of suitable spin-lock we left out with high fidelity singlet states. The goodness of the prepared singlet state is measured by the tomographic method as described in Chapter 2.3. The correlation of the singlet state is given by,

$$\langle\rho_s\rangle(t) = \frac{\text{trace}\left[\rho(t)\cdot\rho_s\right]}{\sqrt{\text{trace}\left[\rho(t)^2\right]\cdot\text{trace}\left[\rho_s^2\right]}}, \tag{2.14}$$

In the following we describe preparation of other Bell states from the singlet state in a two-qubit NMR system.

2.3.2 Preparation of other Bell states from singlet states

Other Bell states can be obtained easily from the singlet state:

$$
\begin{aligned}
|S_0\rangle &\xrightarrow{e^{i\pi I_z^1}} |\psi_+\rangle = \frac{1}{\sqrt{2}}(|01\rangle + |10\rangle), \\
|S_0\rangle &\xrightarrow{e^{i\pi I_x^1}} |\phi_-\rangle = \frac{1}{\sqrt{2}}(|00\rangle - |11\rangle), \\
|S_0\rangle &\xrightarrow{e^{i\pi I_x^1}\cdot e^{i\pi I_z^1}} |\phi_+\rangle = \frac{1}{\sqrt{2}}(|00\rangle + |11\rangle).
\end{aligned} \tag{2.15}
$$

The z-rotation in the above propagators can be implemented by using chemical shift evolution for a period of $1/(2\Delta\nu)$, and qubit selective x-rotation can be implemented by using radio frequency pulses[**?**]. Details of dynamical decoupling on the Bell states will be described in the next sections. In order to investigate the decoupling performance, it is necessary to quantify the decay of Bell states with decoupling duration. The Bell states by themselves are inaccessible to macroscopic observables, but can indirectly be detected transforming to observable single quantum coherences [**?**, **?**]. Alternatively, a more detailed and quantitative analysis of Bell states may be carried out using density matrix tomography as described in Chapter2.3. [**?**]. We have utilized the density matrix formalism for the characterization of the Bell states. The goodness of prepared Bell states can be evaluated from the definition of correlation using expressions similar to (2.14). The density matrices for all the four Bell-state have been shown in figure 2.3. We achieved high fidelity Bell states with correlation around 0.99. In the following we have shown the experimental implementations of dynamical decoupling on such entangled states.

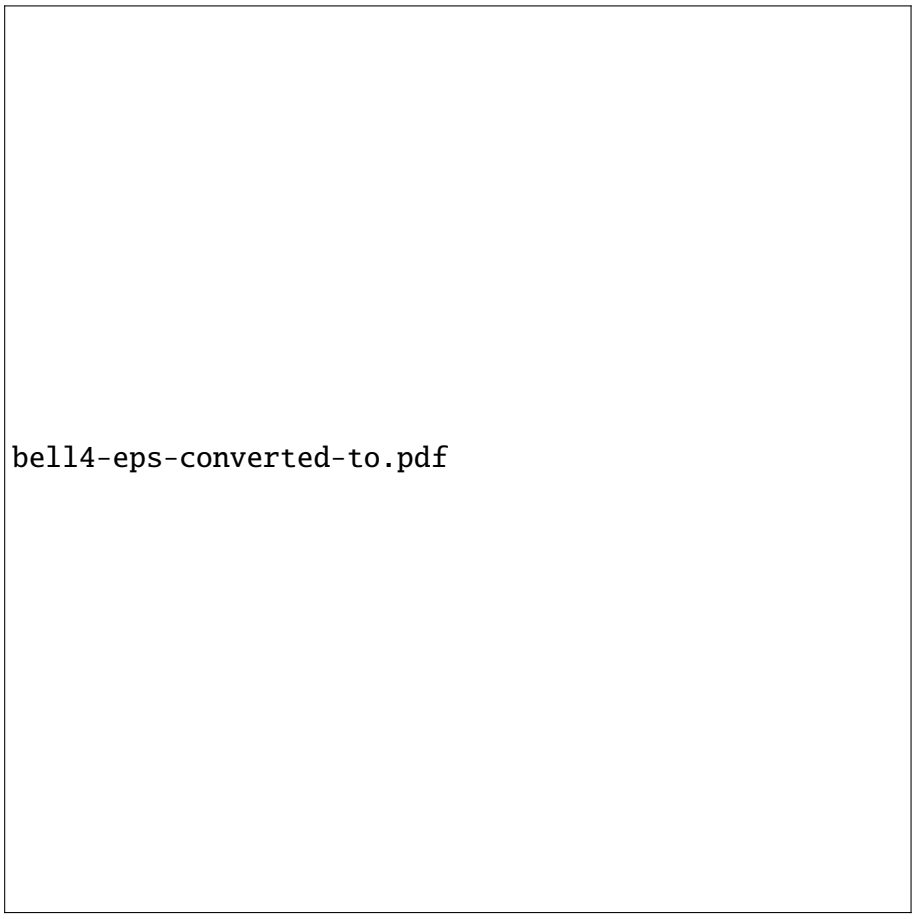

Figure 2.3: Density matrix tomography of Bell states : Real part of (a) singlet state $|S_0\rangle = \frac{1}{\sqrt{2}}(|01\rangle - |10\rangle$ with correlation 0.99, (b) $|\psi_+\rangle = \frac{1}{\sqrt{2}}(|01\rangle + |10\rangle)$ with correlation 0.99, (c) $|\phi_-\rangle = \frac{1}{\sqrt{2}}(|00\rangle - |11\rangle)$ with correlation 0.98, and (d) $|\phi_+\rangle = \frac{1}{\sqrt{2}}(|00\rangle + |11\rangle)$ with correlation 0.97

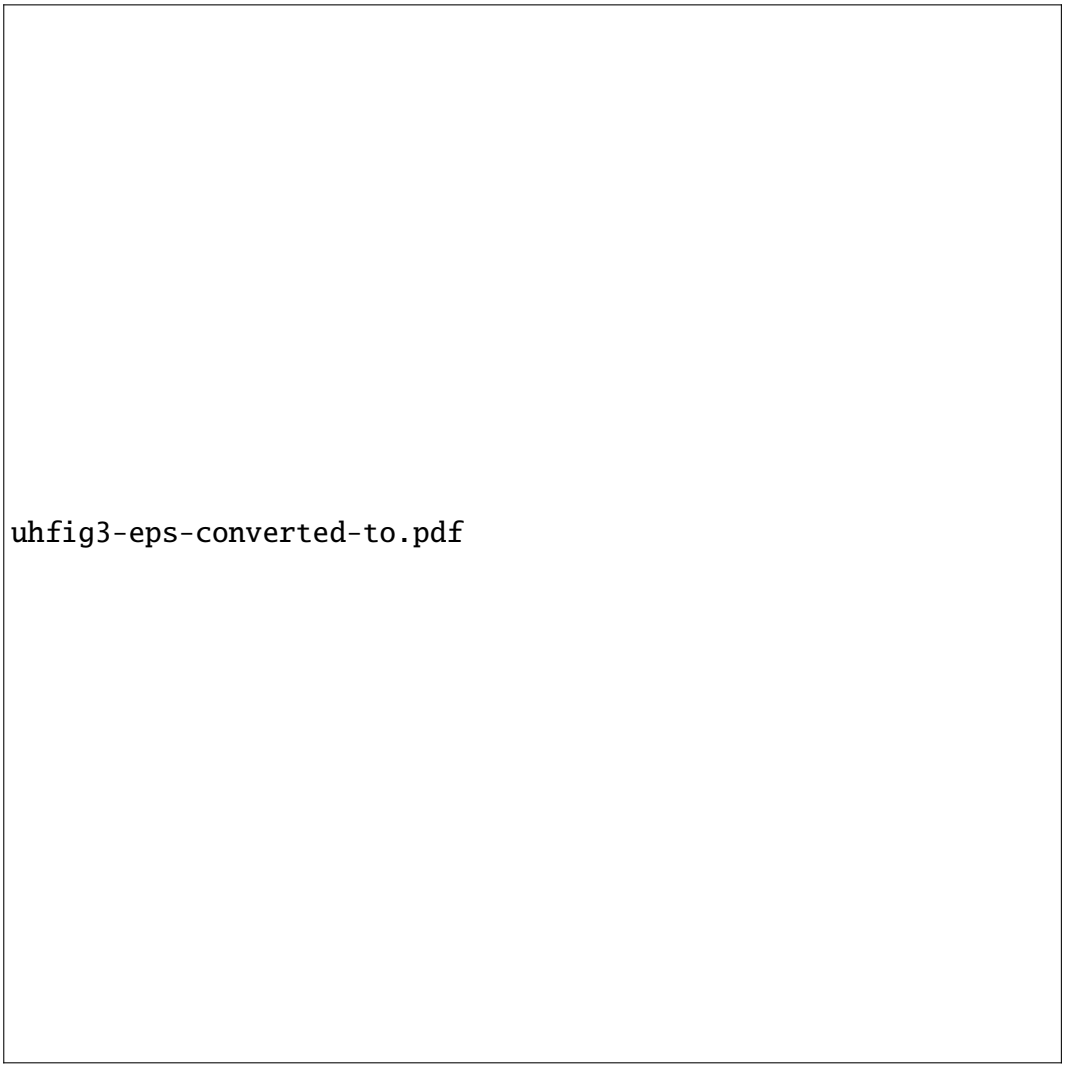

Figure 2.4: Pulse sequences for various orders of Uhrig Dynamical Decoupling. Note that both UDD-1 and UDD-2 are equivalent to CPMG. The time instants are calculated according to the expression (2.8), with N being the order of UDD and the total period $T = N \times 4.0272$ ms.

2.4 Storage of entanglement by UDD

2.4.1 Different orders of UDD

As described earlier, the UDD scheme consists of a sequence of spin flips placed at time instants given by the expression (2.8). Instead of applying the Uhrig's formula for the entire duration of decoupling, we have applied the formula for a short time interval (T) consisting of a small number (N) of pulses and then repeating the sequence. Figure 2.4 shows pulse sequences for various orders of Uhrig Dynamical Decoupling (we refer to an N-pulse UDD sequence as UDD-N). Note that UDD-1 (and UDD-2) are equivalent to CPMG sequences, in which repeating segment consists of $[\tau_{\mathrm{CPMG}} - \pi - \tau_{\mathrm{CPMG}}]$. In our experiments, τ_{CPMG} was set to 2 ms and the duration τ_π of the π pulse was 27.2 μs. The total duration of UDD-N was set to $T = N(2\tau_{\mathrm{CPMG}} + \tau_\pi)$, such that for an extended period of time, the total number of π pulses remain same irrespective of the order of UDD. Only the distribution of π pulses varies according to the order of UDD. For example, in one second of decoupling, there will be about 250 π pulses in all UDD-N. Our investigation thus helps in studying the efficiency of decoupling over a fixed duration of time for a given number of π pulses dispersed according to different orders of UDD.

2.4.2 Performance of UDD over CPMG sequence

Now we describe the performances of UDD-N on the singlet state which was prepared as explained before (see Figure 2.2). After applying UDD-N for a fixed duration of time, we carried out density matrix tomography and evaluated the correlation of the preserved state with theoretical singlet density matrix. The correlations for various orders of UDD are displayed in Figure 2.5. As can be seen from the figure, the singlet state can be preserved for longer durations by UDD-1 (CPMG) than no-decoupling. It is also clear that all even-order UDD sequences result in significant fluctuations in the correlation of the singlet state. However, the odd order UDD preserve the singlet state for tens of seconds. For example, the correlation of the singlet state under UDD-7 at all the sampled

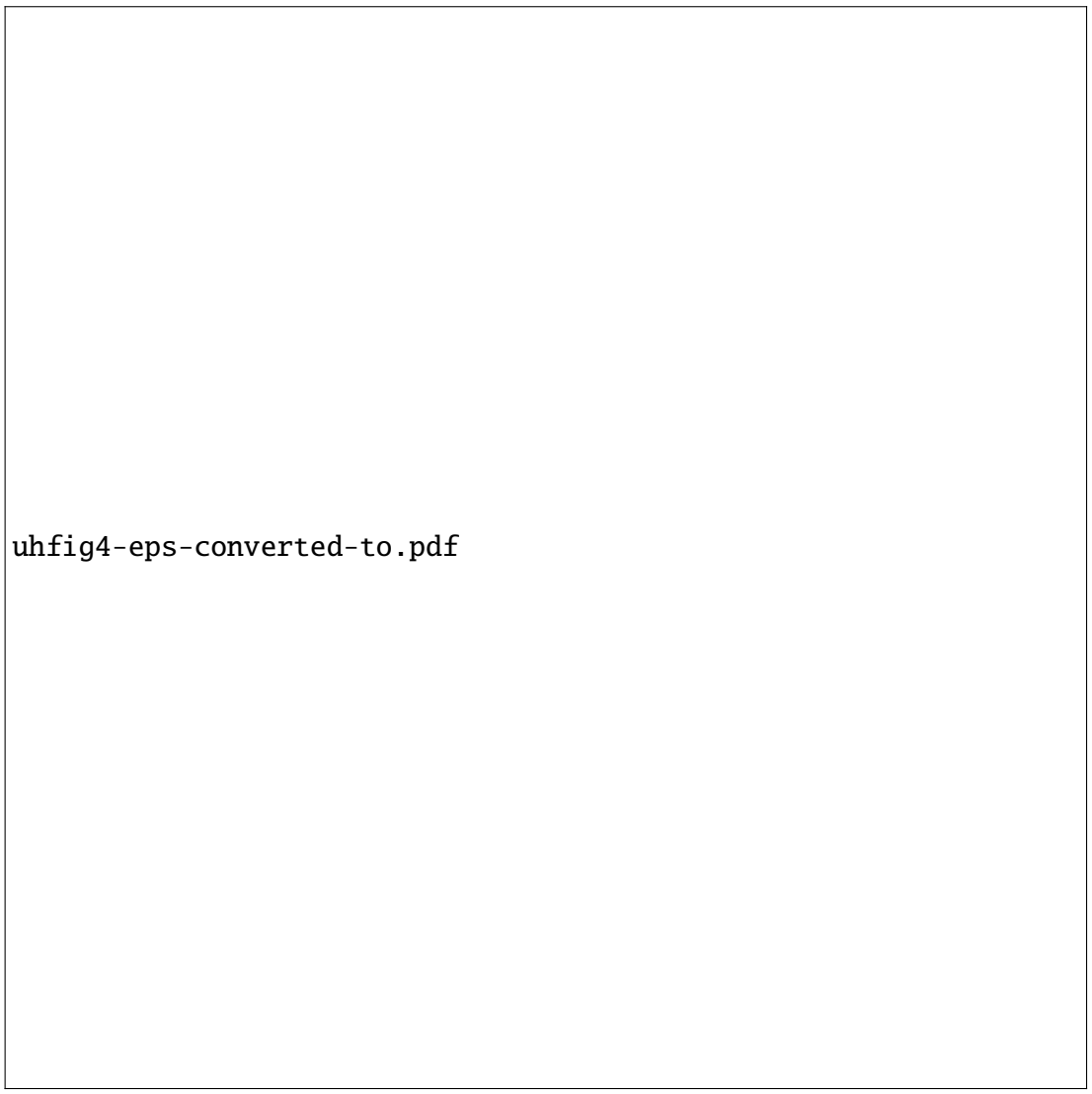

Figure 2.5: Experimental correlations (circles) of singlet state as a function of decoupling duration of various orders of UDD. Also shown in the top-left figure is the correlation decay under no dynamical decoupling (squares).

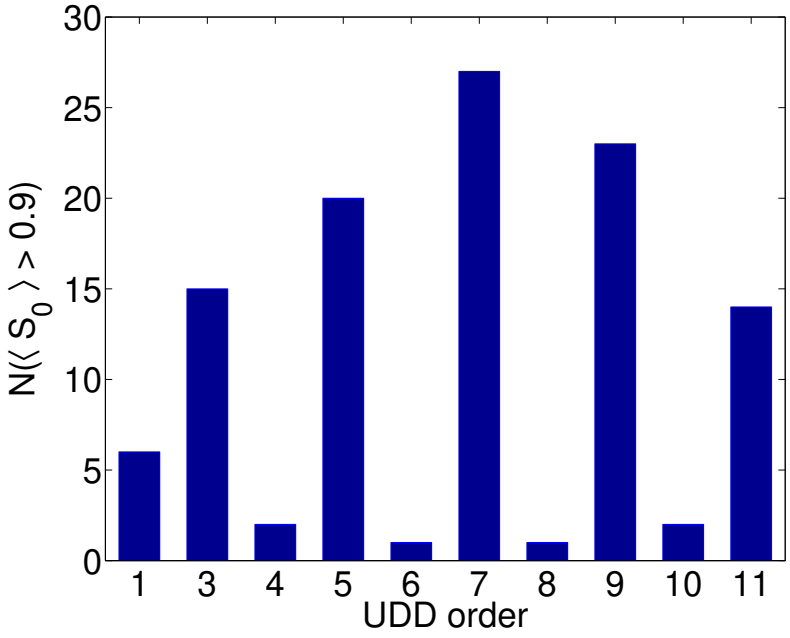

Figure 2.6: The number of time instants at which the correlation exceeded 0.9 for various orders of UDD-N.

time points till 20 seconds is above 0.96. This rather surprising even-odd behavior is likely due to the differences in the performances of the even and odd ordered sequences against the spatial inhmongeneity of the RF pulses.

One way to quantify the efficiency of dynamical decoupling under various orders of UDD in figure 2.5, is by counting the number of time instants in which the correlation of the preserved state exceeds a given threshold. The bar plot in Figure 2.6 compares the number of time instants during decoupling under various orders of UDD in which the correlation of the singlet state exceeded 0.9. It can be seen that there exists an optimal order of UDD (for a given τ_{CPMG} and τ_π), which performs the most efficient decoupling. The optimality may be because of the finite width of the π pulse. In a CPMG sequence the π pulses are uniformly dispersed, while in Uhrig sequence the π pulses are more crowded at the terminals (beginning and ending) of the sequence. For example, if there are too many π pulses, Uhrig's formula will lead to an overlap of pulses. Experimentally, the overcrowding of π pulses may also lead to RF heating of the sample and the probe. Thus the performance of the UDD sequence does not grow

indefinitely with the order of the sequence, but instead will fall beyond a certain order. In our experimental setting, we find that UDD-7 is the optimal sequence for storing the singlet state. There are recent suggestions for decoupling using finite pulses, however these are yet to be studied experimentally [**?**, **?**].

2.4.3 Decay of magnetization during various dynamical decouplings

It can be noticed that the attenuated correlation (expression (2.14)) is insensitive to the decay of the overall magnetization (ϵ in (**??**)), but simply measures the overlap between ρ_Δ and the theoretical density matrix $|\psi\rangle\langle\psi|$. An alternate method is to monitor the decay of magnetization (i.e., ϵ) under dynamical decoupling.

As already mentioned in Chapter 2, singlet state itself can not be measured directly, but can be converted to observable magnetization by using a chemical shift evolution for a duration $1/(4\Delta\nu)$ followed by a $\left(\frac{\pi}{2}\right)_{x(y)}$ pulse. Intensity of the resulting signal as a function of the duration of dynamical decoupling is shown in Figure 2.7. As can be seen, UDD-7 is no better than CPMG in preserving the overall spin-order. In fact the decay constant for CPMG and UDD-7 are 6.1 s and 5.9 s respectively.

2.4.4 Efficiency of UDD over CPMG for a non-entangled state and various Bell states

Now we compare the efficiency of the optimal sequence UDD-7 with UDD-1 (CPMG) for preserving product state ($\sigma_x^1 + \sigma_x^2$) and other Bell states. Figure 2.8 shows the variation of correlation of product states and the Bell states as a function of the decoupling duration [**?**]. Here, after preparing each of the initial state, the dynamical decoupling was applied for a fixed duration of time. To monitor the correlation, we have carried out the density matrix tomography as described earlier [**?**]. In the case of no decoupling, we observe a rapid decay of the correlation. The UDD-1 (CPMG) sequence shows some improvement in the storage time. However, UDD-7 clearly exhibits much longer stor-

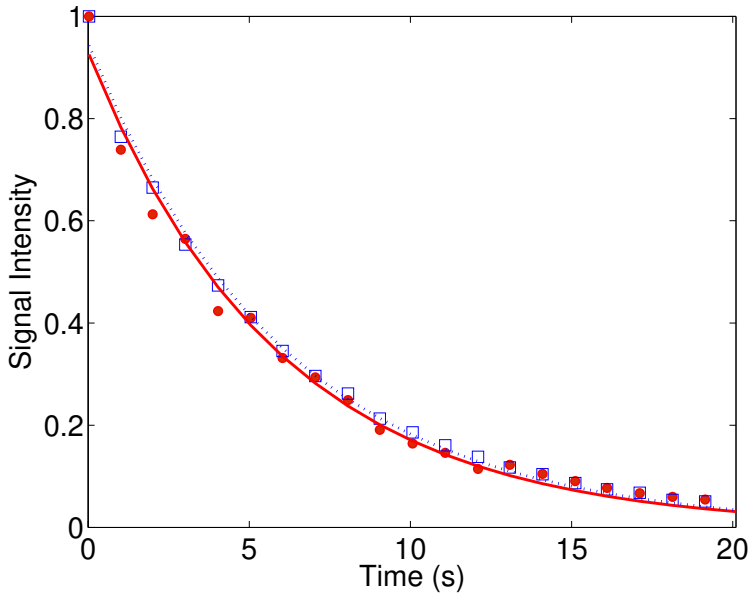

Figure 2.7: The decay of the singlet spin-order measured by converting it into observable single quantum magnetizations. The decay was studied under CPMG sequence (squares) as well as under Uhrig sequence (filled circles). The dashed and the solid line correspond to the exponential fits for CPMG and UDD-7 data points respectively.

age times than the CPMG sequence. The superior performance of UDD-7 on the singlet state compared to other Bell states is presumably because of its antisymmetric property described in section II.

2.5 Conclusions

In this chapter, we have described the effect of decoherence on the quantum system and shows a method to tackle it in practical situations. Dynamical decoupling is a method by which we can reduce the effect of environment on the system and ultimately increase the coherence time scale of the system [**?**]. CPMG is known to be the best known dynamical decoupling sequence both theoretically and experimentally for more than 50 years until 2007. In 2007, Uhrig introduced a new sequence where instead of applying the π pulses at regular intervals, one needs to apply π pulses at irregular intervals synchronizing with a sine-square bell. Theoretically it has been well proved

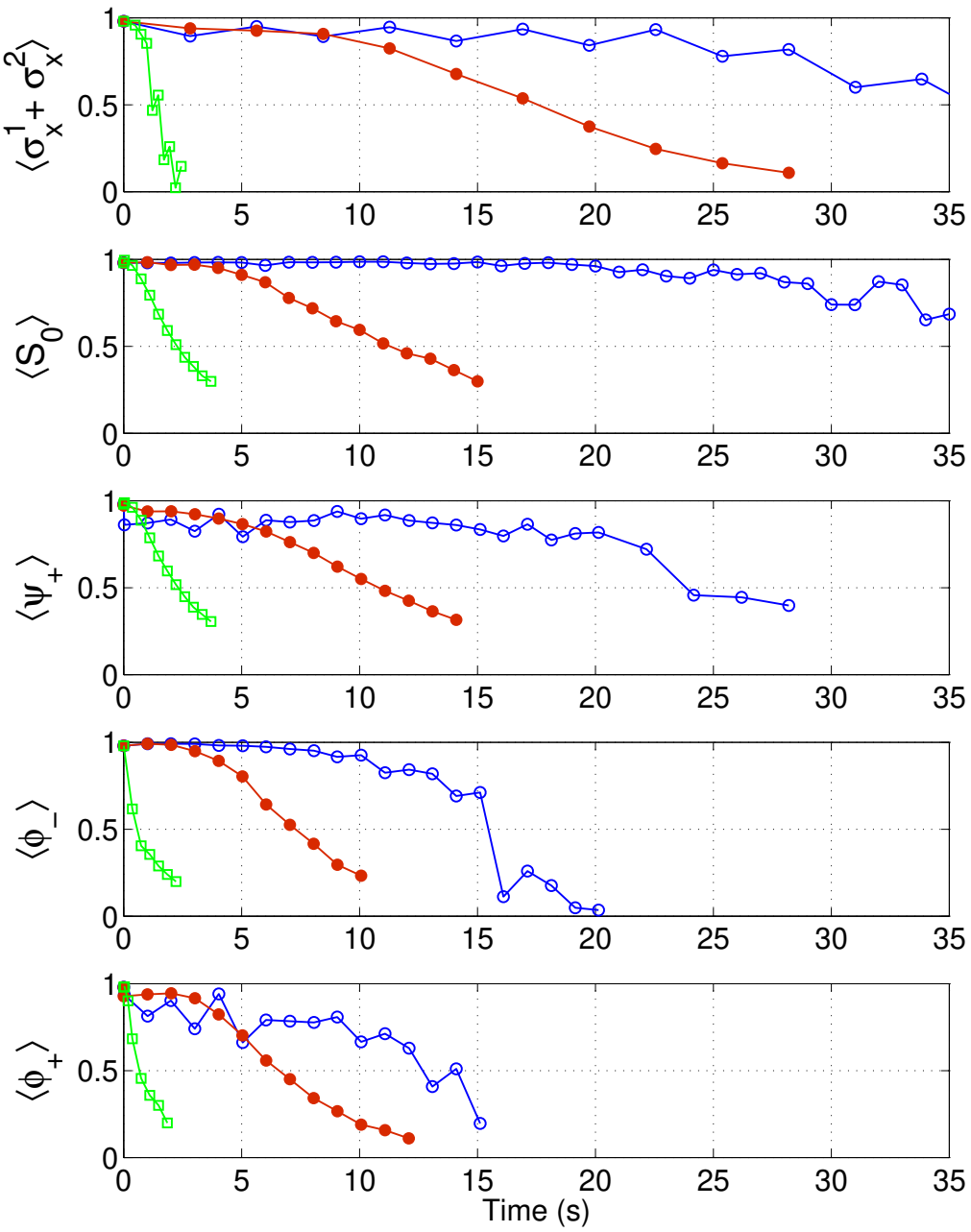

Figure 2.8: Experimental correlations of the product state and various Bell states as a function of duration under (i) no decoupling (open squares), (ii) CPMG sequence (filled circles), and (iii) UDD-7 (open circles).

that Uhrig dynamical sequence (UDD) performs better than CPMG sequence for saving coherence orders of a quantum system. The coherence order for an entangled state is also proved to be elongated by the application of UUD sequence compared to CPMG sequence. Stroboscopic spin flips have already been shown to prolong the coherence times of quantum systems under noisy environments. Uhrig's dynamical decoupling scheme provides an optimal sequence for a quantum system interacting with a dephasing bath. Several experimental demonstrations have already been verified the efficiency of such dynamical decoupling schemes in preserving single qubit coherences.

Here we have shown the first experimental study of UDD sequence on an NMR system. We have studied the efficiencies of CPMG and UDD sequences on 2-qubit Bell states both in terms of magnetization as well as in terms of correlation decay [**?**]. While the Uhrig sequence is no better than CPMG sequence in terms of preserving the overall magnetization (or spin order), it clearly outperforms the CPMG sequence in preserving the correlation of the entangled as well as non-entangled states. We summarize three important features:

(i) The even-order UDD sequences result is fluctuations in correlations.

(ii) The odd-order UDD sequences out-perform the CPMG sequence.

(iii) There exists an optimal length for the odd order UDD sequence which exhibits the most efficient decoupling.

In our case, UDD-7 of 28.2 ms duration appeared to outperform all other sequences of both lower and higher orders. Further understanding on the subject can be achieved by carrying out investigations into the effects of other experimental issues like RF inhomogeneity, resonance off-set, errors in calibration of pulse angle etc. These considerations may help in the theoretical and practical understanding of the optimal decoupling schemes.

Chapter 3

Violation of Leggett-Garg Inequality

In this chapter, we have performed experimental implementation of a protocol for testing the Leggett-Garg inequality (LGI) for nuclear spins in a NMR setup. The motivation and importance of this work is given in the introduction section 3.1. In section 3.2, we have laid out the mathematical formulation of Leggett-Garg inequality for a spin-1/2 nucleus in external magnetic field. In section 3.3, we have presented the Moussa protocol for evaluating the expectation values of a target operator using an ancilla qubit. Section 3.4 shows the experimental results for the 3-qubit and 4-qubit measurements respectively. The conclusion is given in section 3.5.

3.1 Introduction

Distinguishing quantum from classical behavior has been an important issue since the development of quantum theory [**?**, **?**, **?**, **?**, **?**]. This issue is also at the heart of physical realizations of quantum information processing (QIP) [**?**]. Experimental tests for confirming quantumness in physical systems are usually guided by the Bell-type inequalities (BI) [**?**] and the Leggett-Garg inequality (LGI) [**?**]. BI places bounds on certain combinations of correlation coefficients corresponding to measurement outcomes for space-like separated systems which are assumed unable to influence one another (*local*

realism). LGI, on the other hand, places bounds on combinations of temporal correlation coefficients between successive measurement outcomes for a system. Here the system at any instant of time is assumed to be in one or the other of many possible states, and each measurement is assumed to be perfectly non-invasive, in the sense that it has no effect on system's subsequent dynamics (*macrorealism*). In other words, violation of LGI indicates that the system's dynamics cannot be understood in classical terms. In recent years various protocols for implementing LGI and its refined versions have been proposed and experimentally demonstrated [**?**, **?**, **?**, **?**, **?**, **?**, **?**].

Here we have implemented the LGI protocol for individual spin-1/2 nuclei (from a liquid NMR sample) precessing in magnetic field and interacting with their local environments. A typical spin-1/2 system is genuinely 'microscopic' and exhibits quantum behavior. However, it is well-known that, due to decoherence, microscopic quantum systems appear to behave classically and as a consequence QIP tasks relying on such candidate systems tend to fail [**?**]. Nuclear spins from an NMR sample are examples of microscopic quantum systems that are in constant interaction with their local environment and are also candidate systems for QIP tasks. The interactions such as dipole-dipole and chemical-shift anisotropy are known to be leading to decoherence, dissipation and relaxation processes within the spin ensemble [**?**]. In experimental set-ups such as NMR, successful QIP implementation therefore demands confirmation of 'survival' of and determination of 'durability' of quantumness in candidate systems. While an LGI test was originally proposed for addressing the fundamental question about the ability of a *macroscopic* system to behave quantum mechanically, considering its basic mathematical framework, we extend such a test to investigate survival and durability of quantumness within individual nuclear spins interacting with their environments. The investigation also sheds light on the possible consistency of the assumptions of macrorealism with the 'decoherence perspective' [**?**].

Although individual nuclear spins from an NMR sample are not directly address-

able, the sample provides an easily accessible ensemble of nuclear spins from a large number of molecules. Therefore the experimental evaluation of a particular temporal correlation involves *simultaneous* implementations of the LGI protocol on a large number of nuclei (identical 'targets'). Further, an NMR read-out is an 'ensemble average' obtained in terms of magnetization signal. One thus needs to relate the required temporal correlation from an LG string with the NMR signal. A quantum network for encoding correlation between measurement outcomes of a target system in the phase of a probe system has recently been proposed by Moussa *et al* [**?**]. With this network they were able to demonstrate quantum contextuality using nuclear spins from a solid state NMR sample. In this chapter, we exploit this network for testing LGI.

Experimental results shown for values of LG-strings containing three and four temporal correlations as functions of delay between successive measurements [**?**]. We have found good agreement between the quantum mechanically expected and experimentally observed values of the strings for short timescales over which the decay in correlations due to typical NMR relaxation processes are ineffective. Further, to demonstrate effect of decoherence on the state of individual target nuclei which leads to relaxation of the entire ensemble, we have also measured the values of LG strings over longer timescales and found that the LG strings gradually decay and ultimately fall within the classical bounds.

3.2 Leggett-Garg inequality

Consider a system (the 'target') whose state-evolution in time is governed by a particular Hamiltonian. To perform an LGI test for the system, a particular system-observable (say $\mathbb{Q}$) that can be taken as 'dichotomic', i.e. having two possible states with measurement outcomes $Q = \pm 1$, requires to be identified. Next, from a set of 'n' measurement instants $\{t_1, t_2, t_3, ..., t_n\}$, pairs of instants t_i and t_j, such that $j = i+1$, and a pair containing the first ($i = 1$) and the last ($j = n$) instants are to be chosen. For each such pair, one is then required to perform measurements of $\mathbb{Q}$ on the target system at the corresponding

two instants and obtain outcomes $Q(t_i)$ and $Q(t_j)$. After repeating these two-time measurements over a large number of trials (say, N), one can obtain the two-time correlation coefficient (TTCC) C_{ij} for each pair given by the formula:

$$C_{ij} = \frac{1}{N} \sum_{r=1}^{N} Q_r(t_i) \cdot Q_r\left(t_j\right). \tag{3.1}$$

where, r is the trial number. Finally, the values of these coefficients are to be substituted in the n-measurement LG string given by:

$$K_n = C_{12} + C_{23} + C_{34} + ... + C_{(n-1)n} - C_{1n}. \tag{3.2}$$

Each coefficient from the r.h.s. of the above LG string would have a maximum value of $+1$ corresponding to perfect correlation, a minimum value of -1 corresponding to perfect anti-correlation, and 0 for no correlation. Thus, the upper bound for K_n consistent with *macrorealism* comes out to be $(n-2)$, the lower bound is $-n$ for *odd* n, and $-(n-2)$ for *even* n. With these considerations the LGI reads $-n \leq K_n \leq (n-2)$ for odd n, and $-(n-2) \leq K_n \leq (n-2)$ for even n. For example, $-3 \leq K_3 \leq 1$ and $-2 \leq K_4 \leq 2$.

3.2.1 Spin-1/2 precession

The Zeeman Hamiltonian for the precession of a spin-1/2 nucleus in a magnetic field about z-axis, is given by $\hat{H} = \frac{1}{2}\omega\hat{\sigma}_z$, with ω being the angular precession frequency and $\hat{\sigma}_z$ the Pauli-z operator. For the present work we choose the Pauli-x operator, i.e. $\hat{\sigma}_x$, as the dichotomic observable. The quantum mechanical expression of C_{ij} for $\hat{\sigma}_x$ measurements on the nucleus is given by [**?**]

$$C_{ij} = \left\langle \hat{\sigma}_x(t_i)\, \hat{\sigma}_x\left(t_j\right) \right\rangle \approx \cos\left\{\omega(t_j - t_i)\right\}. \tag{3.3}$$

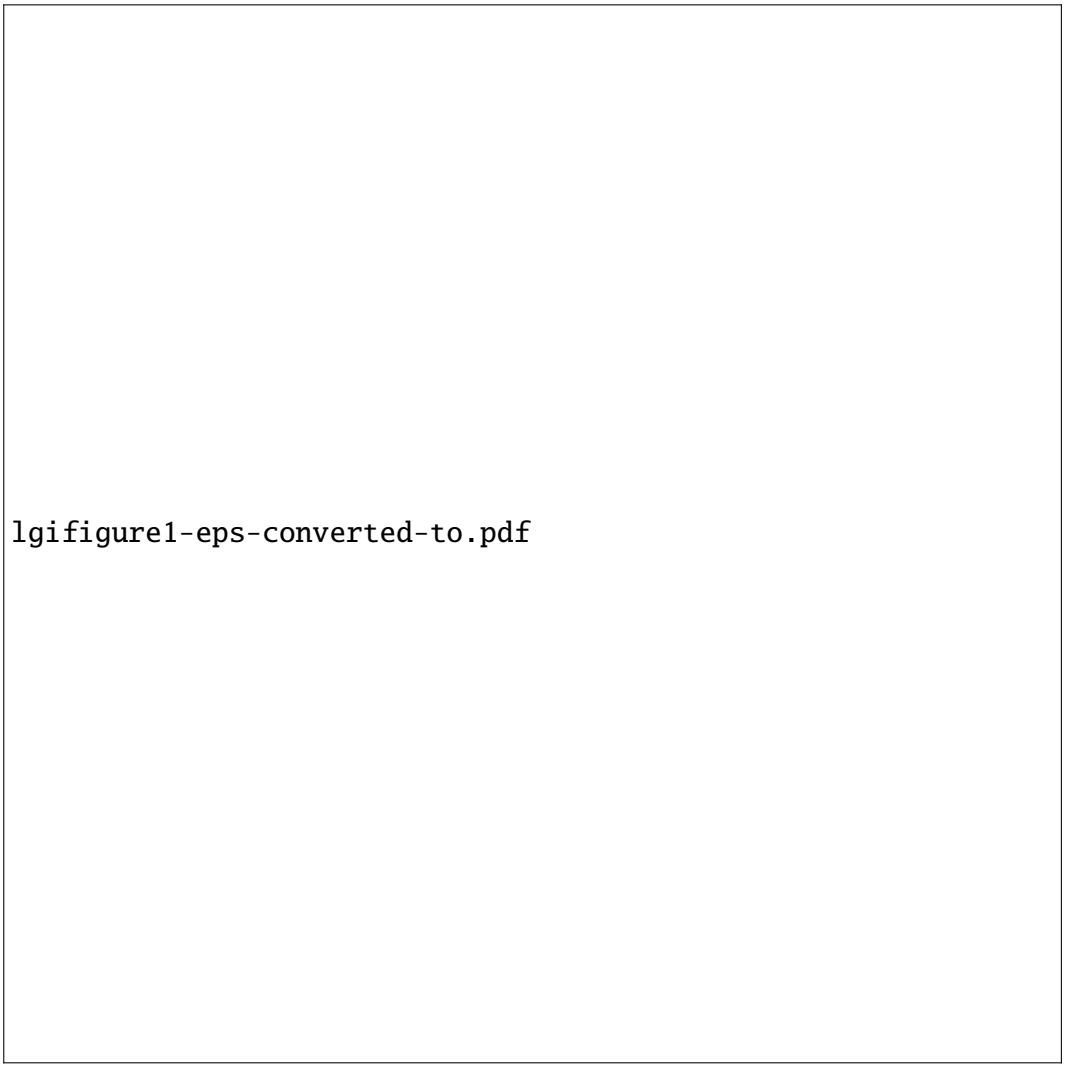

Figure 3.1: The protocols for evaluating $K_3 = C_{12} + C_{23} - C_{13}$ (a) and $K_4 = C_{12} + C_{23} + C_{34} - C_{14}$ (b). In (a) three independent pairs of measurements are used to evaluate TTCCs C_{12}, C_{23}, and C_{13}. Similarly (b) uses four pairs of independent measurements to evaluate C_{12}, C_{23}, C_{34}, and C_{14}.

In Heisenberg representation one can obtain this relation from:

$$C_{ij} \approx \frac{1}{2} \sum_k \left[{}_z\langle k|\hat{\sigma}_x(t_i)\hat{\sigma}_x(t_j)|k\rangle_z \right]. \tag{3.4}$$

Here, $|k\rangle_z \in \{|0\rangle, |1\rangle\}$, is an eigenstate of the Pauli-z operator. If we divide the total duration from t_1 to t_n into $(n-1)$ equal intervals of duration Δt, we can express the LG string consistent with equation (3) as

$$K_n = (n-1)\cos\{\omega\Delta t\} - \cos\{(n-1)\omega\Delta t\}. \tag{3.5}$$

The protocols for evaluating K_3 and K_4 are illustrated in Fig. 3.1. It can be seen that the quantum bounds for K_3 and K_4 are $[-3, +1.5]$ and $[-2\sqrt{2}, +2\sqrt{2}]$ respectively.

3.3 Evaluating TTCCs using network proposed by Moussa et al

Suppose that we wish to evaluate correlations between the outcomes of repeated measurements of two commuting dichotomic unitary observables S_1 and S_2 for a target system (T). Consider an ancilla qubit (called 'probe' P) and a unitary transformation for the joint system 'T + P' ,

$$U_S = \mathbb{I}_{\mathrm{P}} \otimes (P_+)_{\mathrm{T}} + (\hat{\sigma}_z)_{\mathrm{P}} \otimes (P_-)_{\mathrm{T}}. \tag{3.6}$$

Here P_+ and P_- are the projectors onto the eigenspace of $S \in \{S_1, S_2\}$, such that $S = (P_+)_{\mathrm{T}} - (P_-)_{\mathrm{T}}$.

Using equation 3.6, it can be shown that the ensemble measurement of the 'probe' gives correlation between successively measured commuting observables of the 'target'. For evaluating TTCC's from an LG string, the observable-set for the target qubit is $\left\{\hat{\sigma}_x(t_i), \hat{\sigma}_x(t_j)\right\}$ and the corresponding unitaries to be applied to the joint (P + T) system

at different time instants $t_i < t_j$ are

$$U_{\hat{\sigma}_x}(t_q) = \mathbb{I}_P \otimes P_+(t_q) + (\hat{\sigma}_z)_P \otimes P_-(t_q). \tag{3.7}$$

Here $\hat{\sigma}_x(t_q) = P_+(t_q) - P_-(t_q)$ and $q = i, j$ for time instants t_i and t_j. The quantum network for implementing these unitaries is shown in Fig. 3.2(a).

Let the target qubit 'T' be initially prepared according to ρ. If the probe qubit 'P' is initially in one of the eigenstates of the $\hat{\sigma}_x$ operator, say $|+\rangle = (|0\rangle + |1\rangle)/\sqrt{2}$, the density matrix of the joint system is given by

$$(\rho)_{\mathrm{P+T}} = (|+\rangle\langle+|)_P \otimes (\rho)_T. \tag{3.8}$$

Due to the application of the unitaries (7) the joint density matrix evolves according to:

$$(\rho)_{\mathrm{P+T}} \longrightarrow U(t_j, t_i)(\rho)_{\mathrm{P+T}} U^{\dagger}(t_i, t_j) = (\rho')_{\mathrm{P+T}}, \tag{3.9}$$

where $U(t_j, t_i) = U_{\hat{\sigma}_x}(t_j) U_{\hat{\sigma}_x}(t_i)$. In terms of the evolved joint density matrix, the probabilities of obtaining ± 1 outcomes for the Pauli-x measurements on the probe are given by:

$$p(\pm 1) = tr_{\mathrm{P+T}}[(\rho')_{\mathrm{P+T}}\{(|\pm\rangle\langle\pm|)_{\mathrm{P}} \otimes \mathbb{I}_{\mathrm{T}}\}]. \tag{3.10}$$

By tracing over the probe states and using eqns. (3.7 - 3.9) in eqn. 3.10, one obtains:

$$p(\pm 1) = tr_{\mathrm{T}}[\left\{P_+(t_i)P_{\pm}(t_j) + P_-(t_i)P_{\mp}(t_j)\right\}(\rho)_T]. \tag{3.11}$$

The ensemble average of the measurement outcome of joint (P + T) observable is given by:

$$\langle(\hat{\sigma}_x)_{\mathrm{P}} \otimes \mathbb{I}_{\mathrm{T}}\rangle = +p(+1) - p(-1). \tag{3.12}$$

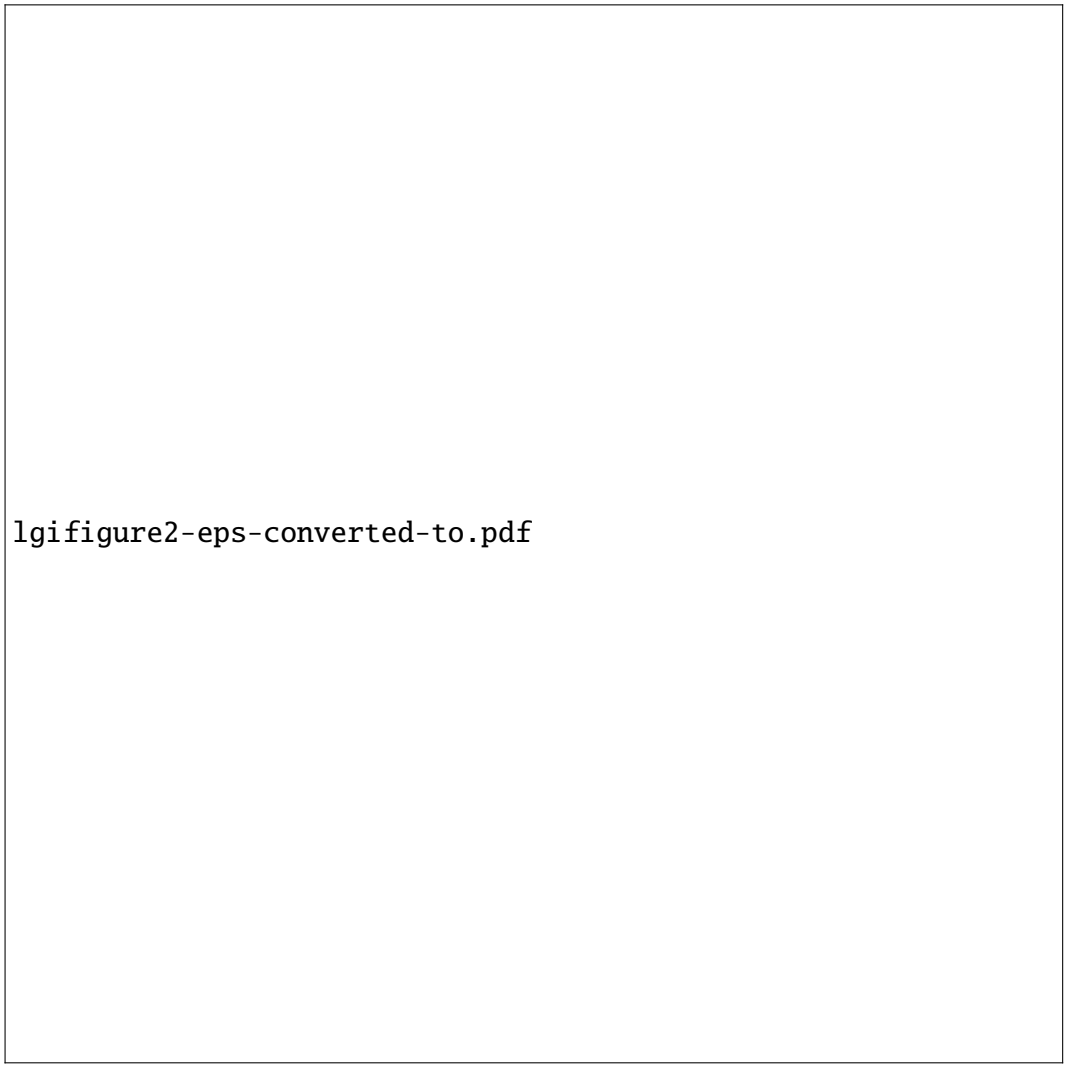

Figure 3.2: Quantum network for the evaluation of TTCCs (a) and the corresponding NMR pulse sequence (b). The ensemble was initially prepared according to $(\rho)_{\mathrm{P}} \otimes (\rho)_{\mathrm{T}}$, where $(\rho)_{\mathrm{P}} = (1 - \epsilon_P)\mathbb{I}/2 + \epsilon_P|+\rangle\langle+|$, and $(\rho)_{\mathrm{T}} = (1 - \epsilon_T)\mathbb{I}/2 + \epsilon_T|+\rangle\langle+|$. Here $\epsilon_{P/T}$ is a dimensionless quantity which represents the purity of the initial states.

Substitution of results 3.11 in equation 3.12 gives:

$$\begin{aligned} \langle(\hat{\sigma}_x)_{\mathrm{P}} \otimes \mathbb{I}_{\mathrm{T}}\rangle &= tr_{\mathrm{T}}[\hat{\sigma}_x(t_i)\hat{\sigma}_x(t_j)(\rho)_T] \\ &= \left\langle \hat{\sigma}_x(t_i)\hat{\sigma}_x(t_j) \right\rangle = C_{ij}. \end{aligned} \tag{3.13}$$

Comparing equations 3.1 and 3.13, it is clear that each TTCC in an LG string can be evaluated by applying unitaries (7) to the joint (probe + target) system followed by an ensemble measurement of Pauli-x operator on the probe.

3.4 Experiment

NMR sample consisted of 2 mg of ^{13}C labeled chloroform ($^{13}CHCl_3$) dissolved in 0.7 ml of deuterated dimethyl sulphoxide (DMSO). To implement the protocol described above, the spin-1/2 nuclei of ^{13}C and ^{1}H atoms are treated as the target spin and the probe spin respectively. All the experiments are carried out on a Bruker 500 MHz spectrometer at an ambient temperature of 300 K. The carbon RF offset was chosen such that the ^{13}C spin precesses at an angular frequency of $\omega = 2\pi \times 100$ rad/s under the effective longitudinal field in the rotating frame of the RF. The proton RF offset was chosen at the resonance frequency of ^{1}H spin. The indirect spin-spin coupling constant (J) for these two spins is 217.6 Hz. The spin-lattice (T_1) and spin-spin (T_2) relaxation time constants for ^{1}H spin are respectively 4.1s and 4.0 s. The corresponding time constants for ^{13}C are 5.5 s and 0.8 s.

The NMR pulse sequence for evaluating TTCCs is described in Fig. 3.2(b). Initial 90 degree y-pulses on both probe and target prepares them in $\hat{\sigma}_x$ states. All the spin manipulations including the C-NOT gates corresponding to $U_{\hat{\sigma}_x}$ operation are realized by specially designed strongly modulated pulses [**?**, **?**] having Hilbert-Schmidt fidelity of over 0.995. These RF pulses are designed to be robust against the RF field inhomogeneity in the range of 90% to 110% and static field inhomogeneity in the range of −5 Hz to +5 Hz. The evolution of J-coupling during the intervals between the measure-

ments are refocused using π pulses on ^{1}H spin. Collective transverse magnetization of the probe spins induce an observable emf on a resonant Helmholtz-type coil which is amplified, digitized and stored as the probe signal. Quadrature detection of the probe signal enables us to measure the x-component of the probe magnetization as the real part of the complex signal. After Fourier transform, the probe signal is fitted to a mixed Lorentzian line shape to extract the absorptive content. A reference signal was obtained by an identical experiment with $\Delta t = 0$. The correlation $C_{ij}(\Delta t)$ was measured at each value of Δt by normalizing the real part of the probe signal with the reference signal. Below, first we will prove the dichotomic nature of nuclear spin observable which is a requisite for the experimental verification of LGI violation. Later subsections shows the experimental results corresponding to LGI violations.

3.4.1 Confirmation of dichotomic nature of x-component of nuclear spin observable

As the first step towards the implementation of any LGI protocol, one needs to identify a *dichotomic* observable for the target system - i.e. having only two possible outcomes scalable as ± 1 - for measurements of which temporal correlations are to be evaluated. Although Pauli-spin operators (relevant to systems such as spin-1/2 nuclei) are routinely taken as dichotomic observables in NMR-QIP implementations, LGI test requires ensuring that this indeed is the case *experimentally*, despite the presence of dominant couplings of the target nucleus with its environment.

The ^{1}H and ^{13}C spins in chloroform are coupled by indirect spin-spin interaction (J) with a strength of 217 Hz. The Hamiltonian for such a two-spin system in a doubly rotating interaction frame can be written as

$$\mathcal{H} = h\nu_H\sigma_z^H/2 + h\nu_C\sigma_z^C/2 + hJ\sigma_z^H\sigma_z^C/4,$$

where ν_H and ν_C are the precession frequencies of the two nuclei [**?**]. In the present

experiment $\nu_H = 0$ Hz and $\nu_C = 100$ Hz. The energy level diagram of such a system is shown in Figure 3.3a. The experimental spectrum of ^{1}H spin consists of two lines corresponding to the two eigenstates of the ^{13}C spin (and vice-versa) (Figure 3.3b-c). The effect of the probe spin (i.e., ^{1}H) on ^{13}C can be removed by spin-decoupling. Under decoupling, the ^{13}C spectrum displays just a single line (Figure 3.3e) corresponding to a two-level system (Figure 3.3d).

We have also recorded the real part of the intensity of signal corresponding to x-magnetization of ^{13}C spin (proportional to $\langle\sigma_x^C\rangle$), under ^{1}H decoupling, as a function of precession duration (Figure 3.4). The data clearly fits to a cosine oscillation of single frequency.

Thus, given the above confirmations that ^{13}C spin is indeed a two-level system and the intensity of its signal corresponding x-magnetization has a cosine oscillation with a single frequency, we can say that σ_x observable used for testing LGI in the present work is dichotomic.

3.4.2 Violation of LGI for 3 measurement case

The 3-measurement LG string $K_3 = C_{12} + C_{23} - C_{13}$ was evaluated for $\omega\Delta t$ varying from 0 to 60π, with Δt incremented from 0 to 300 ms in 360 equal steps. The results of the experiment are shown in Fig. 3.5. The maximum random errors in these experiments were found to be about 0.5%. It is clearly seen that the experimental K_3 data points violate the classical limit and hence macrorealism. Fig. 3.5e shows the K_3 plot for an extended duration consisting of 30 periods. It can be observed that the experimental values of K_3 gradually decay at a time constant of about 288 ms predominantly due to T_1 and T_2 relaxations and due to inhomogeneities in the magnetic field, thus eventually falling within the classical limit for $\omega\Delta t > 26\pi$ (≈ 42 ms).

3.4.3 Violation of LGI for 4 measurement case

Similarly, the 4-measurement LG string K_4 was measured for $\omega\Delta t$ varying from 0 to 16π (i.e., for 8 periods), with Δt varying from 0 to 80 ms. The results of the experiment are shown in Fig. 3.7. Unlike the 3-measurement case, where the classical and quantum mechanical lower limits for K_3 values match (i.e., -3), the 4-measurement case displays violation of the classical limit both in the positive as well as in the negative sides. Similar to the previous case, we observe an exponential decay of K_4 with a time constant of about 324 ms. Decay of LG strings is faster than the measured T_2 values of either spins mainly because T_2's have been measured using CPMG sequences which suppress the effects of static field inhomogeneity and local fluctuating fields.

3.5 Conclusion

The present investigation of LGI employs an ensemble of nuclear spins and alleviates the need for repeated experiments on single isolated systems [**?**]. Simultaneous implementation of controlled operations on target-probe pairs enables evaluation of TTCCs and hence plotting of LG strings as functions of two-time measurement delays. The plots exhibit both violation and satisfaction of LGI respectively for delays shorter than and comparable to the relaxation timescales [**?**]. we qualitatively interpret them as follows: For time scales, over which environmental effects on spin states are negligible, individual target spins can be taken as isolated quantum systems. The plots do reflect this fact in terms of violation of LGI. However, the spin-environment interaction tends to destroy phase relationship characterizing superposition of quantum states of the target nuclear spin. As a result, each member from the ensemble, with its respective environment traced out, begins to appear as if pre-existing in either one of the two states (of a spin observable chosen for performing measurements, which is Pauli-x in the present work) but not in their *superposition*. Such a gradual transition from quantum to *macro-realistic* behavior of individual *microscopic* systems manifests itself in terms of decay of

TTCCs. This ultimately leads to the satisfaction of LGI. Our experimental results thus not only demonstrate initial macrorealism-violating dynamics in genuine microscopic systems such as individual nuclear spins, but also bring forward their environment-induced emergent macrorealistic behavior, captured in terms of satisfaction of LGI and consistent with decoherence mechanism.

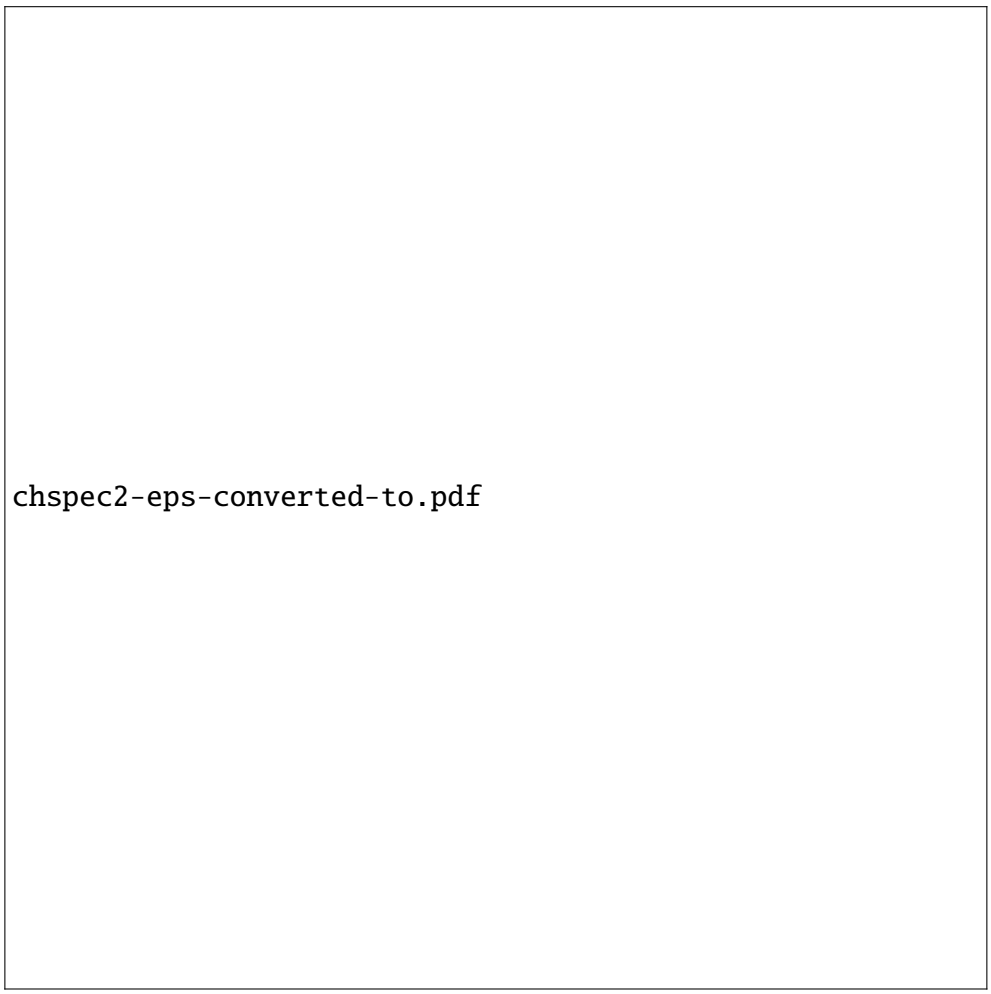

Figure 3.3: The energy level diagram of ^{1}H-^{13}C system (a) displaying four levels corresponding to two coupled spin-1/2 particles, NMR spectra of ^{1}H (b) and ^{13}C (c) nuclei showing splitting due to mutual interactions. The energy levels of ^{13}C spin system after decoupling ^{1}H spin (d), and the corresponding ^{13}C spectrum (e).

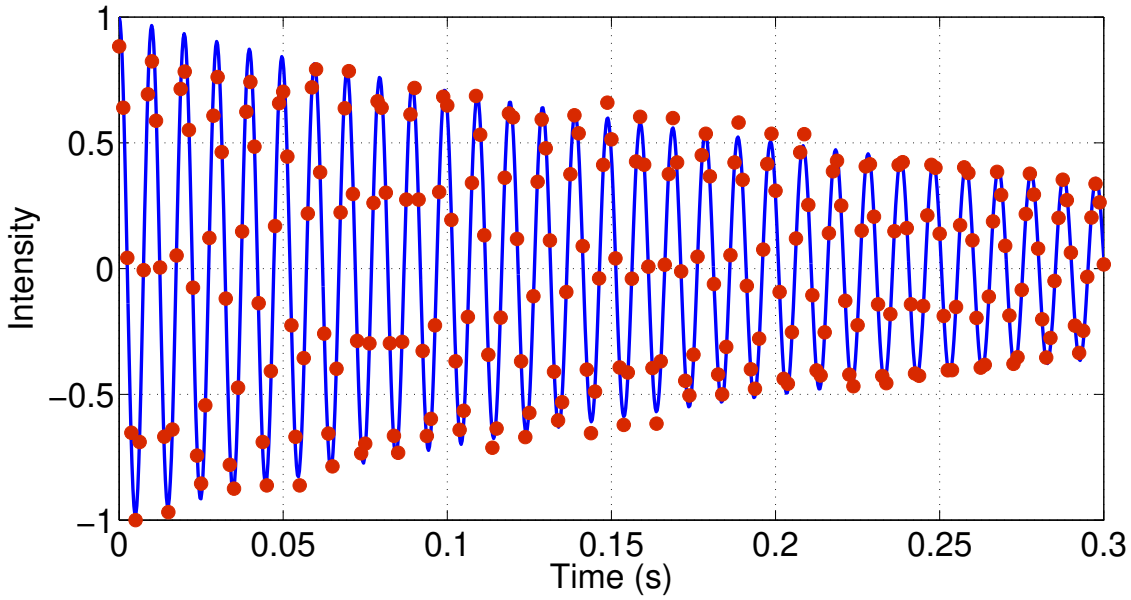

Figure 3.4: Intensity of ^{1}H decoupled ^{13}C spectrum as a function of time. Offsets of the rotating frame are adjusted such that ^{1}H has zero precession frequency and ^{13}C has a precession frequency of 100 Hz. The continuous line is the cosine fit to the experimental data points (dots).

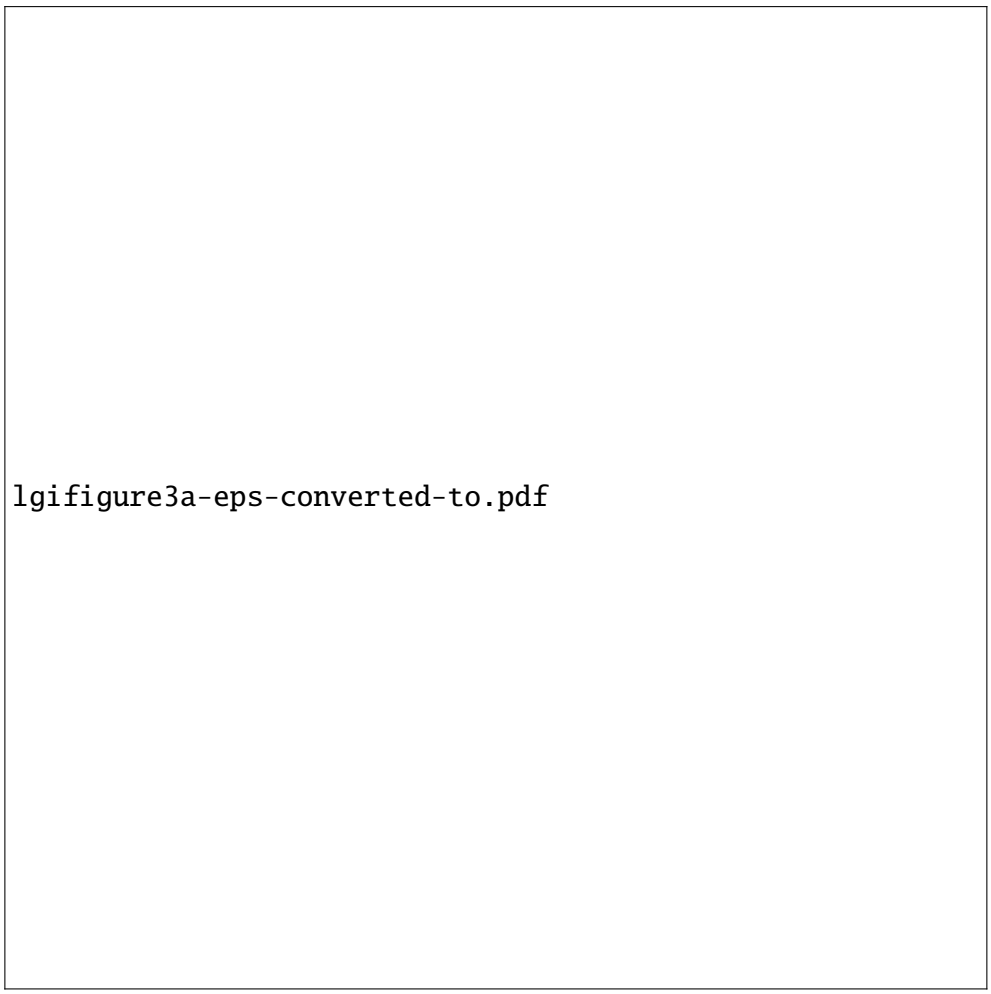

Figure 3.5: Correlations versus Δt: C_{12} (a), C_{23} (b), and C_{13} (c). K_3 is plotted for the range $\omega\Delta t \in [0, 4\pi]$ (d). Continuous lines are theoretically expecting plots with an exponential decay constant and crosses are experimentally achieved results at various time points. The horizontal line in (d) demarcate the boundary between the classical and the quantum regimes.

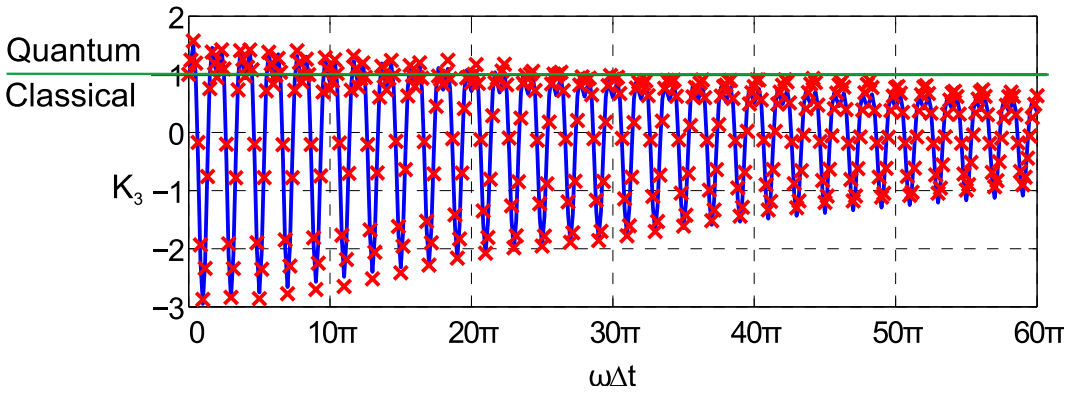

Figure 3.6: Decay of K_3 w. r. t. time: K_3 is plotted for the range $\omega\Delta t \in [0, 60\pi]$. Continuous lines and crosses are used for theoretical (K_3 with decay) and experimental values respectively. The theoretical line was obtained by numerically fitting the K_3 function given in (3.5) with an exponential decay to the experimental data. The horizontal line demarcate the boundary between the classical and the quantum regimes.

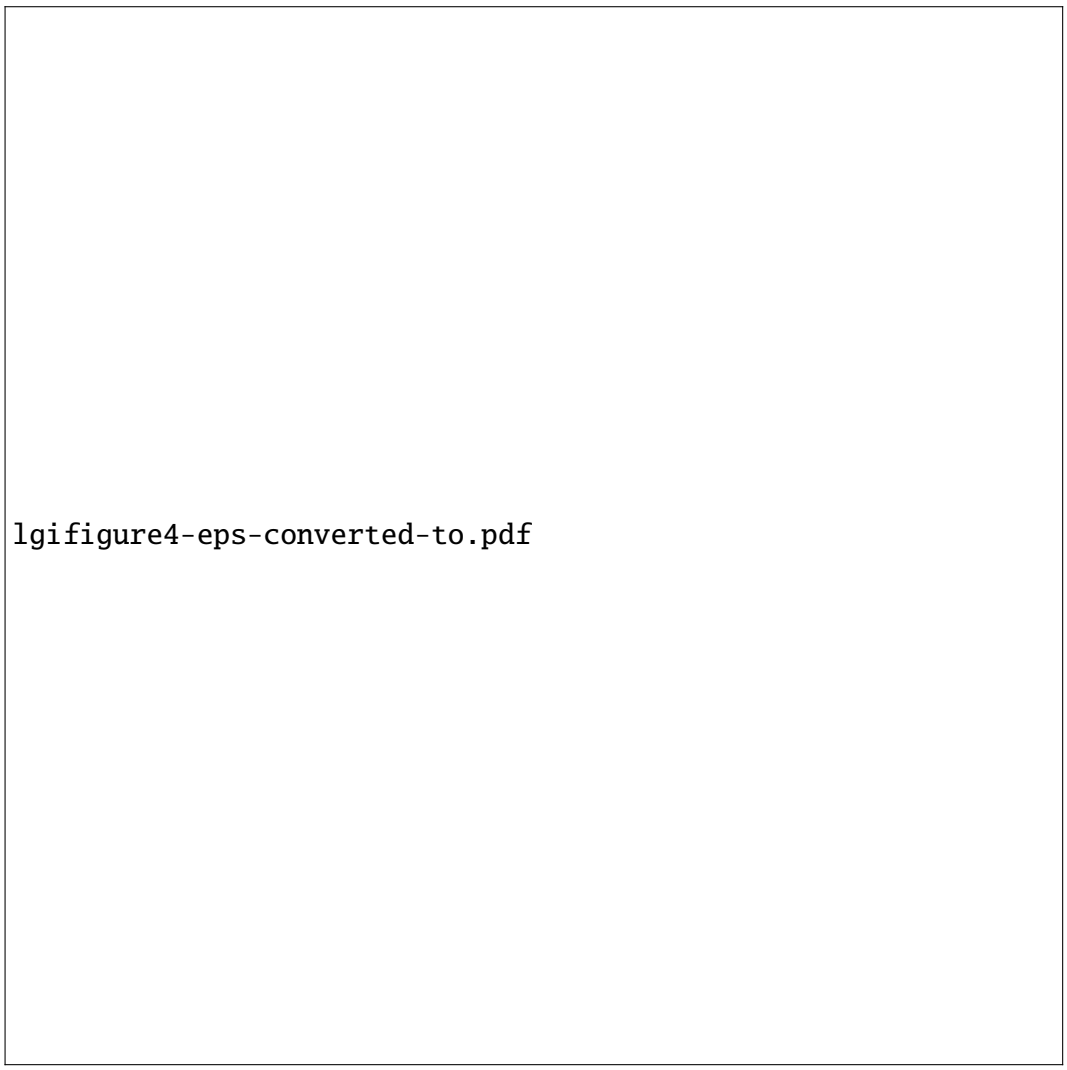

Figure 3.7: The individual correlations C_{12}, C_{23}, C_{34}, and C_{14} are plotted in (a-d) and $K_4 = C_{12} + C_{23} + C_{34} - C_{14}$ is plotted in (e) for the range $\omega\Delta t \in [0, 16\pi]$. Continuous lines and crosses are used for theoretical (K_4 with decay) and experimental values respectively. The theoretical line was obtained by numerically fitting the K_4 function given in (3.5) with an exponential decay to the experimental data. The horizontal line demarcate the boundary between the classical and the quantum regimes.

Chapter 4

Quantum Delayed-Choice Experiment

In this chapter, we have discussed Bohr's complementary principle and its implication on light quanta and subsequently on quantum systems. After giving a short introduction of wave-particle duality in section 4.1, we discussed the various interferometer that is been used to study this strange property in section 4.2. Then we described the theory of recently proposed quantum delayed choice experiment in section 4.3. In section 4.4, we have shown the experimental approach for the implementation of quantum delayed choice circuit in an NMR quantum information processor. The conclusion is given in section 4.5.

4.1 Introduction

"Is light made up of waves or particles?" has been an intriguing question over past many centuries, and the answer remains a mystery even today. The first comprehensive wave theory of light was advanced by Huygens [**?**]. He demonstrated how waves might interfere to form a wavefront propagating in a straight line, and he could also explain reflection and refraction of light. Soon Newton could explain these properties of light using corpuscular theory, in which light was made up of discrete particles [**?**]. The corpuscular theory held over a century till the much celebrated Young's double slit

experiment clearly established the wave theory of light [**?**]. In the Young's experiment, a monochromatic beam of light passing through an obstacle with two closely separated narrow slits produced an interference pattern with troughs and crests just like one would expect if waves from two different sources would interfere. Other properties of light like diffraction and polarization could also be explained easily using the wave theory. The 20th century developments such as Plank's theory of black-body radiation and Einstein's theory of photoelectric effects required quantization of light into photons [**?**, **?**]. But the question remained whether individual photons are waves or particles. Subsequent development of quantum mechanics was based on the notion of wave-particle duality [**?**], which was essential to explain the behavior not only of the light quanta, but also of atomic and sub-atomic entities [**?**].

4.2 Studying wave-particle duality by interferometers

4.2.1 Mach-Zhender Interferometer

The wave-particle duality of quantum systems is nicely illustrated by a Mach-Zehnder interferometer (MZI) (see Fig. 4.1) [**?**, **?**]. The intensity of the incident light is kept sufficiently weak so that photons enter the interferometer one by one. In the open-setup (Fig. 4.1a), it consists of a beam-splitter BS1, providing each incoming photon with two possible paths, named 0 and 1. A phase-shifter in path-1 introduces a relative phase ϕ between the two paths. The two detectors D0 and D1 help to identify the path traveled by the incident photon. Experimental results show that only one of the detectors clicks at a time [**?**]. Each click can then be correlated with one of the two possible paths by attributing particle nature to the photons. Here the phase-shifter has no effect on the intensity of the photons measured by either detector, and therefore no interference is observed in this setup.

In the closed-setup (Fig. 4.1b), the interferometer consists of a second beam-splitter BS2, which allows the two paths to meet before the detection. Experimental results

again show that only one detector clicks at a time. But much to the astonishment of common intuition, the results after many clicks do show an interference pattern, i.e., the intensities recorded by each detector oscillates with ϕ [**?**]. Since only one photon is present inside the interferometer at a time, each photon must have taken both paths in the interferometer and therefore this setup clearly establishes the wave property of photons.

The naive question by the classical mindset is "whether the photon entering the interferometer decides to take one of the paths or both the paths depending on the experimental setup?". Scientists who believed in a deterministic nature had proposed that, unknown to the current experimentalist, there exists some extra information about state of the quantum system, which in principle dictates whether the photon should take either path, or both the paths [**?**]. In other words, they assumed some hidden information availed by the photon coming out of BS1 about the existence or non-existence of BS2.

4.2.2 Wheeler's delayed-choice experiments

In order to break this causal link between the two beam-splitters, Wheeler proposed a modification in the MZI setup (Fig. 4.1c), in which the decision to introduce or not to introduce BS2 is to be made after the photon has already passed through BS1 [**?**, **?**, **?**]. This way, there is no causal connection between the selection of the paths by the photon and the presence of BS2. Although initially considered as a 'thought-experiment', this proposal has recently been demonstrated by Jacques et al [**?**]. In their experimental setup, the second beam-splitter (RBS) was controlled by a random number generator (RNG), that choose to switch the beam-splitter ON or OFF after the photon has already passed through BS1. The results of this delayed-choice experiment was in agreement with Bohr's complementarity principle [**?**]. That is, the behavior of the photon in the interferometer depends on the choice of the observable that is measured, even when that choice is made at a position and a time such that it is separated from the entrance of the photon into the interferometer by a space-like interval. Breaking the causal link had no

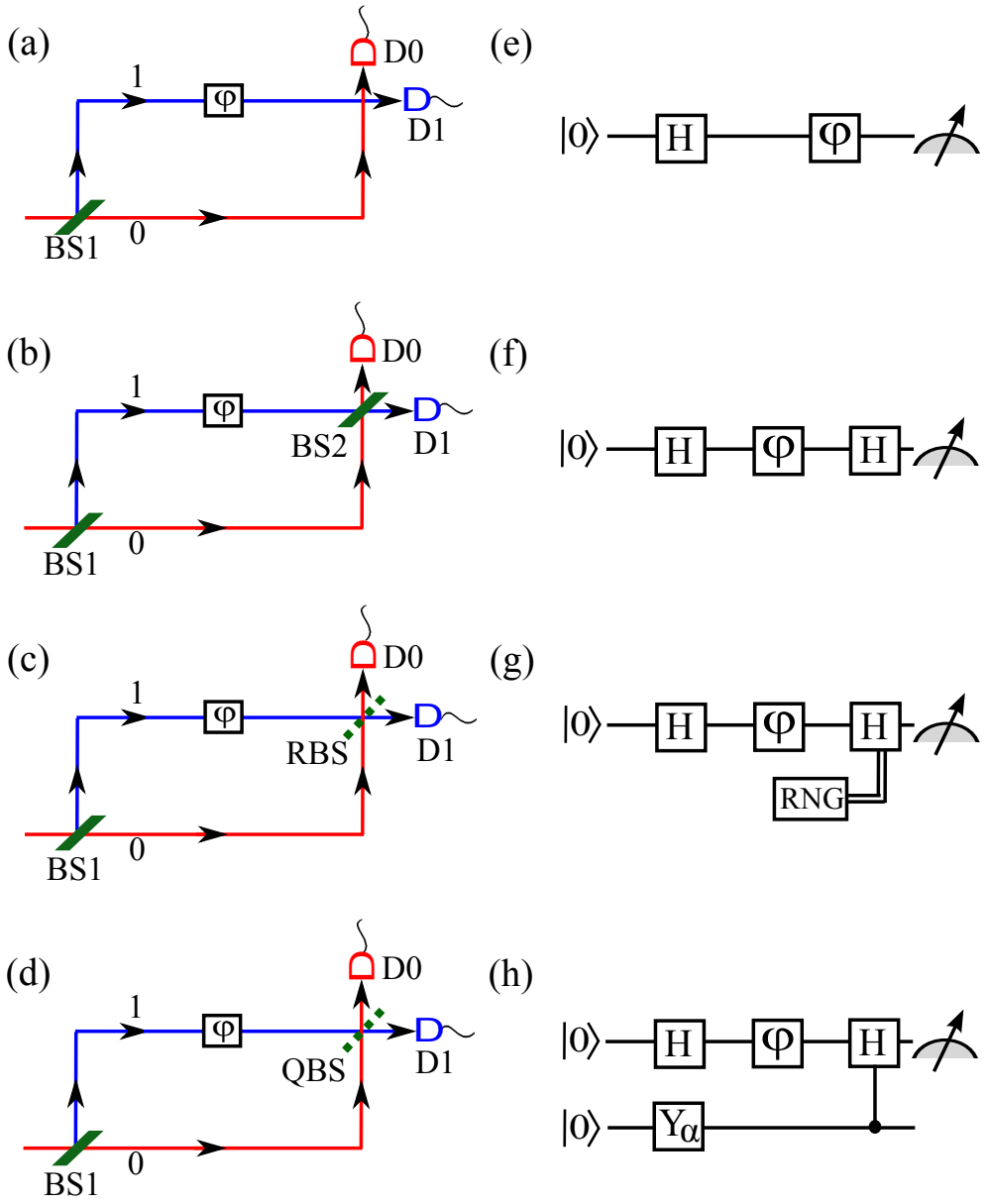

Figure 4.1: Different types of Mach-Zehnder interferometer setups (a-d) and equivalent quantum circuits (e-h). BS1 and BS2 are beam splitters, ϕ is phase shifter, D0 and D1 are detectors. RBS is a beam-splitter switched ON or OFF by a random number generator (RNG) and QBS is a beam-splitter which is controlled by a quantum system in superposition. In the quantum circuits, H is the Hadamard gate and $Y_\alpha = e^{-i\alpha\sigma_y}$ is used to prepare the state of ancilla qubit.

effect on the results of the wave-particle duality, thus ruling out the existence of hidden information [**?**].

4.2.3 Quantum delayed-choice experiments

Recently, Ionicioiu and Terno have proposed a modified version (Fig. 4.1d) of the Wheeler's experiment which not only demonstrates the intrinsic duality, but also shows that a photon can have a morphing behavior between particle and wave [**?**]. In their setup, BS2 is replaced with a beam splitter which is switched OFF or ON depending on $|0\rangle$ or $|1\rangle$ state of a two-level quantum system. Using this modification, Ionicioiu and Terno have been able to discard hidden variable theories which attempt to assign intrinsic wave or particle nature to individual photons even before the final measurement. This proposed experiment is named as 'Quantum Delayed-Choice Experiment' [**?**].

Using nuclear magnetic resonance (NMR) techniques we study the behavior of a target spin-1/2 nucleus going through a similar situation as that of a photon going through an interferometer [**?**]. Another spin-1/2 nucleus acts as an ancilla controlling the second beam-splitter. In section 4.3 we briefly explain the theory and in section 4.4 we describe the experimental results.

4.3 Theory

In the following we shall use the terminology of quantum information. The two possible paths of the interferometer are assigned with the orthogonal states $|0\rangle$ and $|1\rangle$ of a quantum bit. The equivalent quantum circuits for the different setups of MZI are shown in Figs. 4.1(e-h). Similar circuits have previously been used in 'duality computers' [**?**, **?**, **?**]. In these circuits the Hadamard operator H has the function of the beam splitter BS1. It transforms the initial state $|0\rangle$ to the superposition $(|0\rangle + |1\rangle)/\sqrt{2}$ such that both $|0\rangle$ and $|1\rangle$ states are now equally probable. The detection operators for the two detectors are $D_0 = |0\rangle\langle 0|$ and $D_1 = |1\rangle\langle 1|$.

In the open setup (Fig. 4.1e), the state after the phase shift becomes, $|\psi_p\rangle = (|0\rangle + e^{i\phi}|1\rangle)/\sqrt{2}$. The intensities recorded by the two detectors are given by the expectation values,

$$\begin{aligned} S_{\mathrm{p},0} &= \langle\psi_{\mathrm{p}}|D_0|\psi_{\mathrm{p}}\rangle = \frac{1}{2} \text{ and} \\ S_{\mathrm{p},1} &= \langle\psi_{\mathrm{p}}|D_1|\psi_{\mathrm{p}}\rangle = \frac{1}{2}, \end{aligned} \tag{4.1}$$

independent of the phase introduced. Therefore no interference can be observed and accordingly this setup demonstrates the particle nature of the quantum system. The visibility of the interference

$$\nu = \frac{\max(S) - \min(S)}{\max(S) + \min(S)}, \tag{4.2}$$

is zero in this case.

The equivalent quantum circuit for the closed interferometer is shown in Fig. 4.1f. After the second Hadamard one obtains the state, $|\psi_{\mathrm{w}}\rangle = \cos\frac{\phi}{2}|0\rangle - i\sin\frac{\phi}{2}|1\rangle$, up to a global phase. The intensities recorded by the two detectors are now,

$$\begin{aligned} S_{\mathrm{w},0} &= \langle\psi_{\mathrm{w}}|D_0|\psi_{\mathrm{w}}\rangle = \cos^2\frac{\phi}{2} \text{ and} \\ S_{\mathrm{w},1} &= \langle\psi_{\mathrm{w}}|D_1|\psi_{\mathrm{w}}\rangle = \sin^2\frac{\phi}{2}. \end{aligned} \tag{4.3}$$

Thus as a function of ϕ, each detector obtains an interference pattern with visibility $\nu = 1$. This setup clearly demonstrates the wave nature of the target qubit.

In the circuit corresponding to the Wheeler's experiment (Fig. 4.1g), the decision to insert or not to insert the second Hadamard gate is to be made after the first Hadamard gate has been applied.

Here, we focus on the next modification, that is the quantum delayed-choice experiment [**?**]. In the equivalent quantum circuit (Fig. 4.1h), the second Hadamard gate is to be decided in a quantum way. This involves an ancilla spin prepared in a superposition

state $\cos\alpha|0\rangle + \sin\alpha|1\rangle$. This state can be prepared by rotating the initial $|0\rangle$ state of ancilla by an angle 2α about y-axis (using operator $Y_\alpha = e^{-i\alpha\sigma_y}$). The second Hadamard gate is set to be controlled by the ancilla qubit. If the ancilla is in state $|0\rangle$, no Hadamard gate is applied, else if the ancilla is in state $|1\rangle$, Hadamard gate is applied. The combined state of the two-qubit system after the control-Hadamard gate is

$$|\psi_{\mathrm{wp},\alpha}\rangle = \cos\alpha|\psi_{\mathrm{p}}\rangle|0\rangle + \sin\alpha|\psi_{\mathrm{w}}\rangle|1\rangle, \tag{4.4}$$

wherein the second ket denotes the state of ancilla. After tracing out the ancilla, the reduced density operator for the system becomes,

$$\rho_{\mathrm{wp}} = \cos^2\alpha|\psi_{\mathrm{p}}\rangle\langle\psi_{\mathrm{p}}| + \sin^2\alpha|\psi_{\mathrm{w}}\rangle\langle\psi_{\mathrm{w}}|. \tag{4.5}$$

Again, the intensity recorded by each detector can be obtained by calculating the expectation values. For example, the intensity at the detector D0 is,

$$\begin{aligned} S_{\mathrm{wp},0}(\alpha,\phi) &= \mathrm{tr}[D_0\,\rho_{\mathrm{wp}}] \\ &= \mathrm{tr}[D_0|\psi_{\mathrm{p}}\rangle\langle\psi_{\mathrm{p}}|]\cos^2\alpha + \\ &\quad \mathrm{tr}[D_0|\psi_{\mathrm{w}}\rangle\langle\psi_{\mathrm{w}}|]\sin^2\alpha \\ &= S_{\mathrm{p},0}\cos^2\alpha + S_{\mathrm{w},0}\sin^2\alpha \\ &= \frac{1}{2}\cos^2\alpha + \cos^2\frac{\phi}{2}\ \sin^2\alpha. \end{aligned} \tag{4.6}$$

It can be immediately seen that the visibility ν for the above interference varies as $\sin^2\alpha$. When $\alpha = 0$, the quantum system has a particle nature and when $\alpha = \pi/2$, it has a wave nature. In the intermediate values of α, the quantum system is morphed in between the particle and the wave nature. In the following section we describe the experimental demonstration of morphing of a quantum system between wave and particle behaviors.

4.4 Experiment

The sample consisted of $^{13}CHCl_3$ (Fig. 4.2a) dissolved in $CDCl_3$. Here ^{1}H and ^{13}C spins are used as the target and the ancilla qubits respectively. The two spins are coupled by indirect spin-spin interaction with a coupling constant of $J = 209$ Hz. All the experiments were carried out at an ambient temperature of 300 K in a 500 MHz Bruker NMR spectrometer.

4.4.1 Open and closed interferometers

The pulse-sequences corresponding to open and closed setups of MZI are shown in Fig. 4.2(b-c). In these cases, the circuits (Fig. 4.1(e-f)) need only a single target qubit and no ancilla qubit. Here ^{1}H spin is used as the target qubit, and its interaction with ^{13}C spin is refocused during the MZI experiments. Ideally both of these setups need initializing the target qubit to $|0\rangle$ state. In thermal equilibrium at temperature T and magnetic field B_0, an ensemble of isolated spin-1/2 nuclei exists in a Boltzmann mixture,

$$\rho_{\text{eq}} = \frac{1}{2}e^{\epsilon/2}|0\rangle\langle 0| + \frac{1}{2}e^{-\epsilon/2}|1\rangle\langle 1|, \tag{4.7}$$

$\epsilon = \gamma\hbar B_0/kT$ is a dimensionless constant which depends on the magnetogyric ratio γ of the spin. At ordinary NMR conditions $\epsilon \sim 10^{-5}$ and therefore ρ_{eq} is a highly mixed state. Since preparing a pure $|0\rangle$ state requires extreme conditions, one can alleviate this problem by rewriting the equilibrium state as the pseudopure state

$$\rho_{\text{eq}} = |0\rangle\langle 0|_{\text{pps}} \approx \frac{1}{2}\left(1 - \frac{\epsilon}{2}\right)\mathbb{1} + \frac{\epsilon}{2}|0\rangle\langle 0|. \tag{4.8}$$

The identity part does neither evolve under the Hamiltonians, nor does it give raise to NMR signals, and is therefore ignored. Thus the single qubit equilibrium state effectively mimics the state $|0\rangle$.

In all the cases (Fig. 4.2(b-d)), the first Hadamard gate on the target qubit is followed

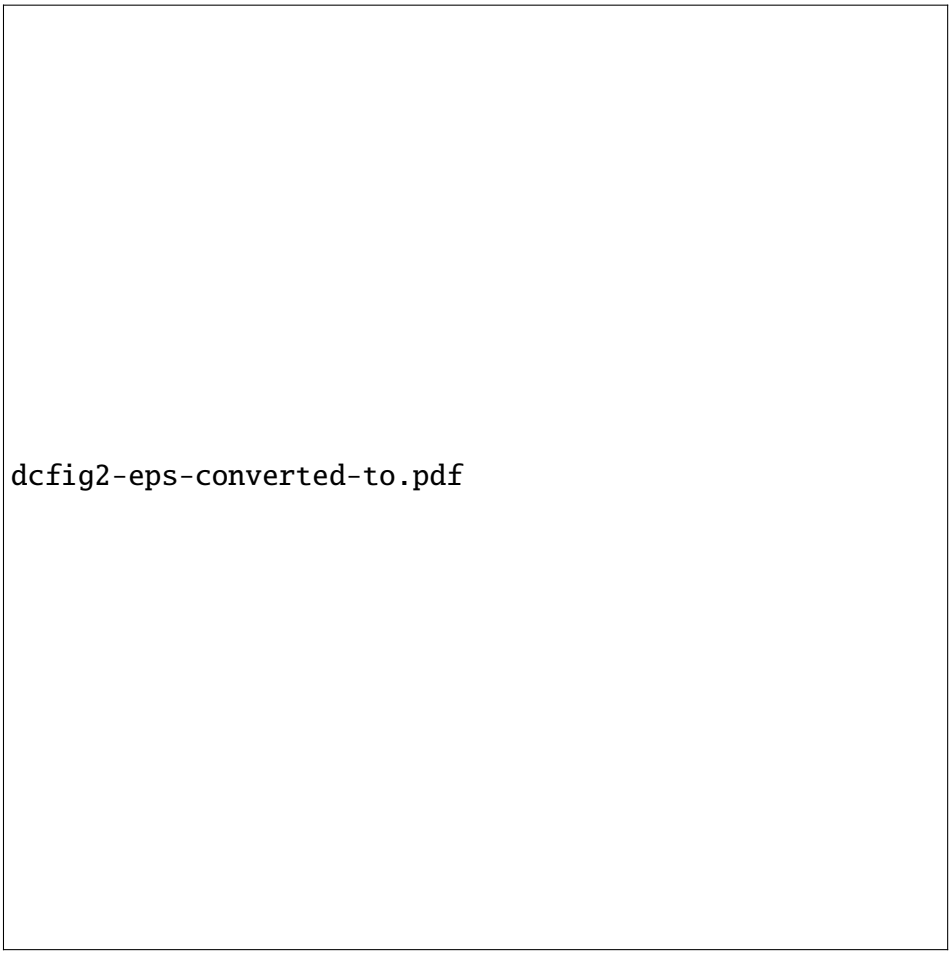

Figure 4.2: Molecular structure of chloroform (a) and pulse-sequences (b-d) for different setups of MZI. Figs. (b) and (c) correspond to the open and closed setups respectively, and (d) corresponds to the quantum delayed-choice experiment. The unfilled rectangles are π pulses. Shaped pulses are strongly modulated pulses corresponding to Hadamard gate (H), Y_α gate, and control-Hadamard (cH) gate. $\pi/2$ detection pulses are shown in dotted rectangles. J is the coupling constant and τ is the phase-shifting delay. G_1 and G_2 are two pulsed-field-gradients for destroying coherences. In (d) two separate experiments for ^{1}H and ^{13}C are recorded after applying respective $\pi/2$ detection pulses. ρ_{eq}, $\rho_p = |\psi_p\rangle\langle\psi_p|$, $\rho_w = |\psi_w\rangle\langle\psi_w|$, and $\rho_{wp} = |\psi_{wp}\rangle\langle\psi_{wp}|$ represent the states at different time instants.

by the phase shift. A 100 Hz resonance off-set of ^{1}H spin was used to introduce the desired phase shift $\phi(\tau) = 200\pi\tau$, with the net free-precession delay τ. Experiments were carried out at 21 linearly spaced values of ϕ in the range $[0, 2\pi]$. The ^{13}C spin was set on-resonance and the J-evolution during τ was refocused with a π pulse on ^{13}C.

Unlike the open interferometer (Fig. 4.2b), the closed interferometer (Fig. 4.2c) has a second Hadamard gate. In both of these cases, the intensity recorded by D1 detector corresponds to the expectation value of $D_0 = |0\rangle\langle 0|$ operator, which is a diagonal element of the density operator. To measure this element, we destroy all the off-diagonal elements (coherences) using a pulsed field gradient (PFG) G_1, followed by a $(\pi/2)_y$ detection pulse. The most general diagonal density operator for a single qubit is $\rho = \frac{1}{2}\mathbb{1} + c\sigma_z$, where c is the unknown constant to be determined. After applying the $(\pi/2)_y$ detection pulse, we obtain $\frac{1}{2}\mathbb{1} + c\sigma_x$. The corresponding NMR signal is proportional to c. The experimental NMR spectra for the open and closed setups are shown in Fig. 4.3. These spectra are normalized w.r.t. equilibrium detection. Since both the pathways created by BS1 are equally probable in the open MZI, $c = 0$ and therefore spectrum vanishes. On the other hand, because of the second beam-splitter (BS2) in closed MZI, c becomes ϕ dependent, and hence the interference pattern.

The corresponding intensities $S_{\mathrm{p(w),0}} = c + 1/2$ are shown in Fig. 4.4. The theoretical values from expressions (4.1) and (4.3) are also shown in solid lines. The experimental visibility of interference in the particle case is 0.02 and that in the wave case is 0.97. As explained in the previous section, the open setup demonstrates the particle nature and the closed setup demonstrates the wave nature.

4.4.2 Quantum delayed-choice experiment

The circuit for quantum delayed-choice experiment is shown in Fig. 4.1h and the corresponding NMR pulse-sequence is shown in Fig. 4.2d. This circuit requires one target qubit (^{1}H) and one ancilla qubit (^{13}C). The equilibrium state of the two-qubit system does not correspond to a pseudopure state and therefore it is necessary to redistribute

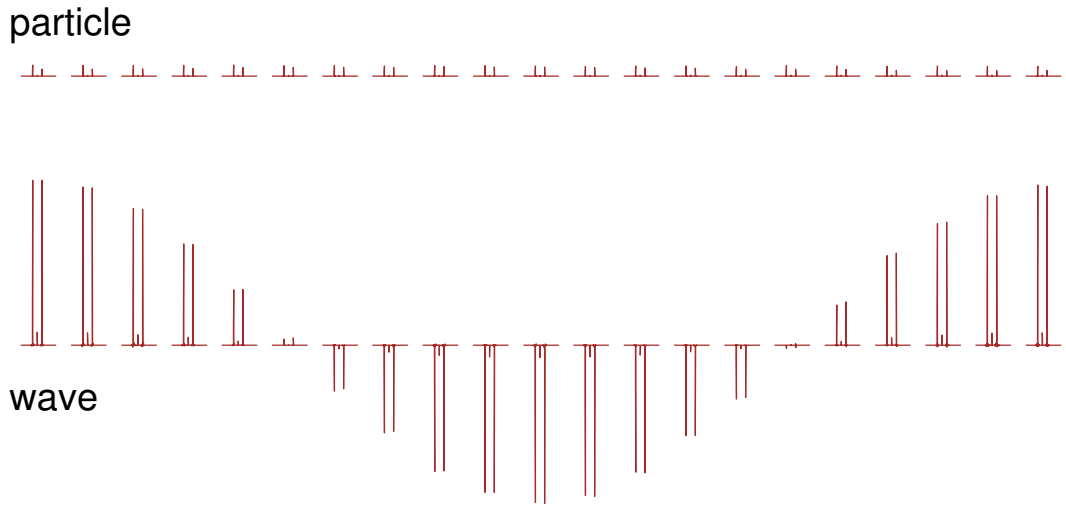

Figure 4.3: The experimental spectra obtained after the open (top trace) and closed (bottom trace) setups of MZI. Each spectrum (pair of lines) corresponds to one of the 21 linearly spaced values of ϕ in the range $[0, 2\pi]$.

the populations to achieve the desired pseudopure state. We used spatial averaging technique to prepare the pseudopure state [**?**]

$$\rho_{\text{pps}} = \frac{1-\epsilon'}{4}\mathbb{1} + \epsilon'|00\rangle\langle 00|, \tag{4.9}$$

where ϵ' is the residual purity.

All the gates on the target and the ancilla were realized using strongly modulated pulses (SMPs) [**?**, **?**]. The SMPs were constructed to be robust against RF amplitude inhomogeneities, which normally have a distribution of about 10 % about the mean. Robust pulses were achieved by calculating the Hilbert-Schmidt fidelity between the desired operator and the experimental operator for different possible RF amplitude distributions, and then maximizing the average fidelity [**?**]. An average fidelity of over 0.995 was achieved for each gate. After the control-Hadamard gate, the state of the two-qubit system is expressed by the density operator ρ_{wp} (eqn. 4.5) up to the unit

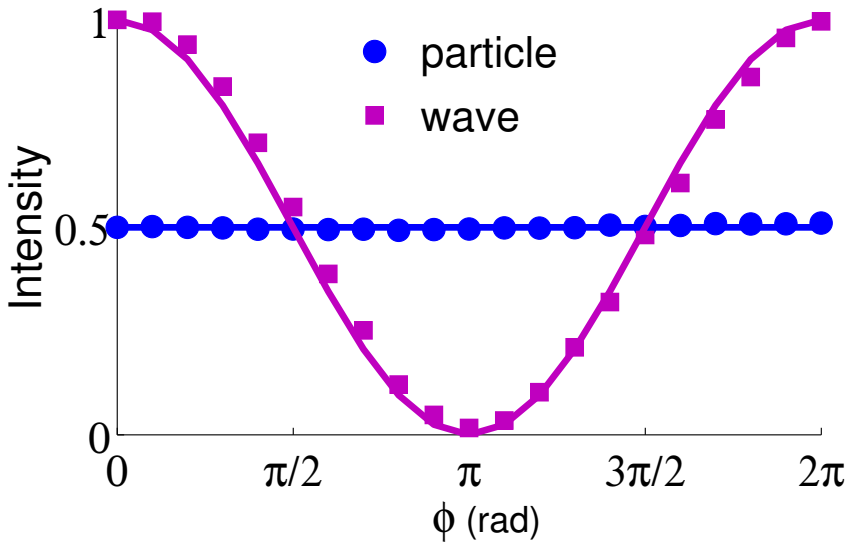

Figure 4.4: The experimental intensities $S_{\mathrm{p},0}$ (particle) and $S_{\mathrm{w},0}$ (wave) at various values of ϕ.

background.

The interference $S_{\mathrm{wp},0}$ (in eqn. 4.6) due to the detection operator $D_0 = |00\rangle\langle 00|$ can be obtained by measuring the first diagonal element of the density matrix, and hence complete density matrix tomography is not necessary [**?**]. As in the single qubit case, we apply a PFG G_2 which averages out all the coherences and retains only the diagonal part of the density matrix. The most general diagonal density matrix of a two-qubit system is of the form

$$\rho = \frac{1}{4}\mathbb{1}\otimes\mathbb{1} + c_1\sigma_z\otimes\mathbb{1} + c_2\mathbb{1}\otimes\sigma_z + c_3\sigma_z\otimes\sigma_z, \tag{4.10}$$

with the unknown constants c_1, c_2, and c_3.

Recording the target spectrum after a $(\pi/2)_y$ pulse on the above state gives two sig-

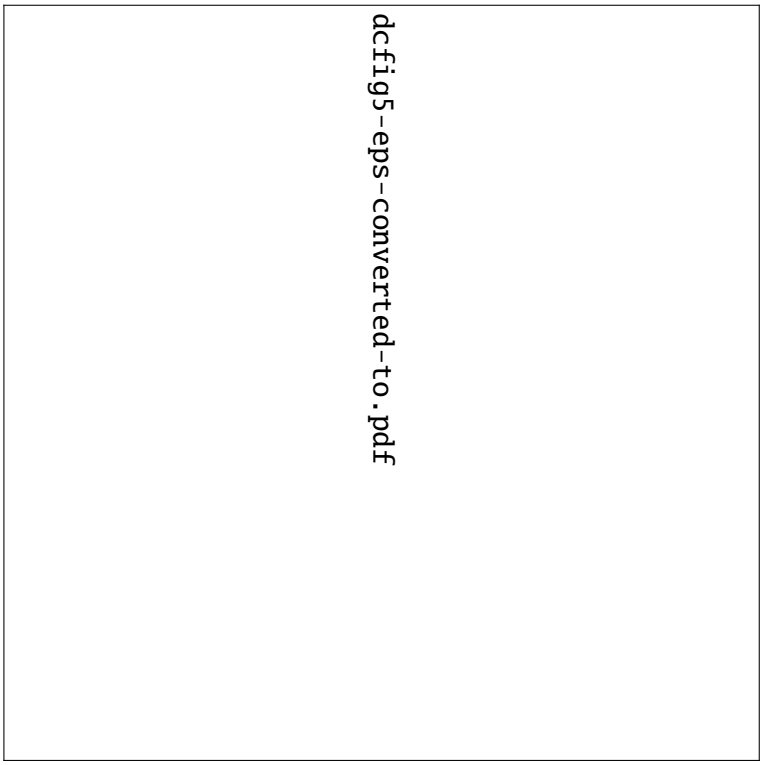

Figure 4.5: The experimental spectra obtained after the quantum delayed choice experiment with $(\pi/2)_y$ detection pulse on target (^{1}H) qubit. These spectra are recorded with 21 equally spaced values of $\phi \in [0, 2\pi]$ and at different α values (as indicated). In each spectrum, only one line is expected due to the preparation of pseduopure state.

nals proportional to $c_1 + c_3$ and $c_1 - c_3$. The spectra of the target qubit at various values of ϕ and α are shown in Fig. 4.5. The signals obtained after applying a $(\pi/2)_y$ pulse on either qubit after preparing the $|00\rangle$ pseudopure state are used to normalize these intensities. In each spectrum, the left transition (corresponding to the $|0\rangle$ state of ancilla), vanishes because of the particle nature (similar to the top trace of Fig. 4.3) and the right transition (corresponding to the $|1\rangle$ state of ancilla) displays the interference pattern because of the wave nature (similar to the bottom trace of Fig. 4.3).

Similarly, recording the ancilla spectrum after a $(\pi/2)_y$ pulse gives two signals proportional to $c_2 + c_3$ and $c_2 - c_3$. From these four transitions one can precisely determine all the three unknowns c_1, c_2, and c_3, and obtain the population $S_{\mathrm{wp},0} = 1/4 + c_1 + c_2 + c_3$. Calculated experimental intensities $S_{\mathrm{wp},0}$ are shown in Fig. 4.6a. The intensities were measured for five values of α in the range $[0, \pi/2]$, and for 21 values of ϕ in the range $[0, 2\pi]$. The theoretical values from expression (4.6) are also shown in solid lines. The experimental values were found to have small random errors with a standard deviation less than 0.01. The significant systematic errors are due to experimental limitations such as radio-frequency inhomogeneity and spectrometer non-linearities.

The visibility ν calculated at different values of α are plotted in Fig. 4.6b. The theoretical visibility varies as $\sin^2 \alpha$ as explained in the section II. There appears a general agreement between the quantum mechanical predication (solid-line) and the experiments (symbols).

4.5 Conclusions

In this chapter, we have studied the open and closed setups of Mach-Zehnder interferometer using nuclear spin qubits, and demonstrated the particle-like and wave-like behaviors of the target qubit. Previously NMR interferometer has been used to study dipolar oscillations in solid state NMR [**?**] and to measure geometric phases in multilevel systems [**?**, **?**, **?**]. We have reported the first experimental demonstration of the quantum delayed-choice experiment using NMR interferometry.

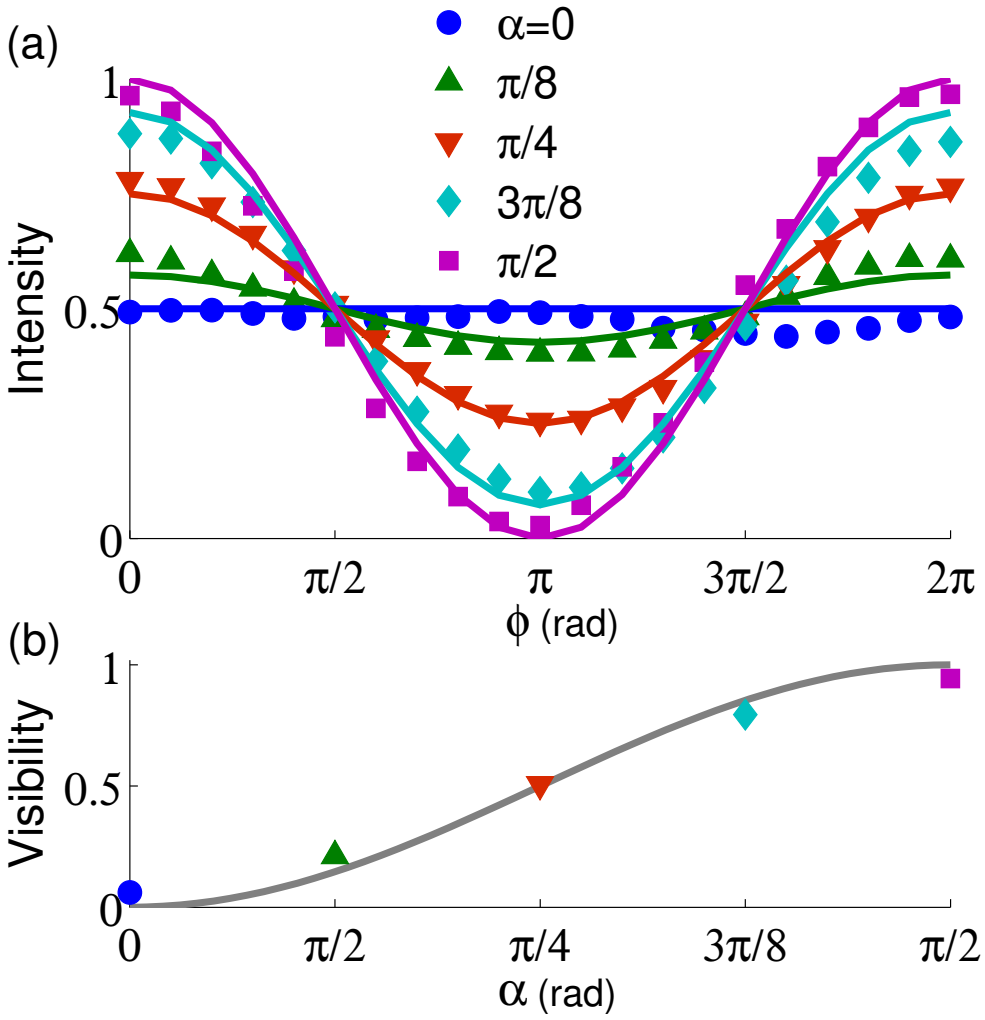

Figure 4.6: The intensities $S_{\mathrm{wp},0}(\alpha,\phi)$ versus phase ϕ for different values of α (a) and the visibility ν versus α (b). The theoretical values are shown in solid lines and the experimental results are shown by symbols.

Bohr's complementarity principle is based on mutually exclusive experimental arrangements. However, the quantum delayed-choice experiment proposed by Ionicioiu and Terno [**?**], suggests that we can study the complementary properties like particle and wave behavior of a quantum system in a single experimental setup if the ancilla is prepared in a quantum superposition. This experiment is the quantum version of the Wheeler's delayed-choice experiment. The quantum delayed-choice experiment suggests a reinterpretation of complementarity principle: instead of complementary experimental setups, the new proposal suggests complementarity in the experimental data.

The NMR systems provide perfect platforms for studying such phenomena [**?**]. In our experiments we found a general agreement between the intensities and the visibilities of the interference with the theoretically expected values. These experiments not only confirm the intrinsic wave-particle duality of quantum systems, but also demonstrates continuous morphing of quantum systems between wave and particle behavior of the target qubit depending on the quantum state of the ancilla qubit.

Chapter 5

Density Matrix tomography for a three spin-1/2 homonuclear system

The method for three-spin tomography is similar to one that we have described for a two-spin system. Since the number of unknowns here for three-spin system is much higher (63 unknowns) than two-spin (15 unknowns) system, we need to have more number of experiments in order to find out all the unknowns faithfully. The 8×8 general density matrix (ρ) for a three-spin system can be written as follows:

$$
\begin{array}{c}
 \\
\langle 000| \\
\langle 001| \\
\langle 010| \\
\langle 011| \\
\langle 100| \\
\langle 101| \\
\langle 110| \\
\langle 111|
\end{array}
\begin{array}{c}
\begin{array}{cccccccc}
|000\rangle & |001\rangle & |010\rangle & |011\rangle & |100\rangle & |101\rangle & |110\rangle & |111\rangle
\end{array} \\
\left(\begin{array}{cccccccc}
P_0 & r_9+is_9 & r_5+is_5 & r_{13}+is_{13} & r_1+is_1 & r_{14}+is_{14} & r_{15}+is_{15} & r_{25}+is_{25} \\
 & P_1 & r_{16}+is_{16} & r_6+is_6 & r_{17}+is_{17} & r_2+is_2 & r_{26}+is_{26} & r_{18}+is_{18} \\
 & & P_2 & r_{10}+is_{10} & r_{19}+is_{19} & r_{27}+is_{27} & r_3+is_3 & r_{20}+is_{20} \\
 & & & P_3 & r_{28}+is_{28} & r_{21}+is_{21} & r_{22}+is_{22} & r_4+is_4 \\
 & & & & P_4 & r_{11}+is_{11} & r_7+is_7 & r_{23}+is_{23} \\
 & & & & & P_5 & r_{24}+is_{24} & r_8+is_8 \\
 & & & & & & P_6 & r_{12}+is_{12} \\
 & & & & & & & \sum_{j=0}^{6} -P_j
\end{array}\right)
\end{array}
\tag{5.1}
$$

The lower triangle of the density matrix can be filled by applying the Hermitian property of it ($\rho_{jk} = \rho^*_{kj}$). The diagonal elements (P_j, $j = 0 \rightarrow 6$) are representing population distributions of the density matrix. Applying the traceless property (or identity trace property), one of the unknowns can be reduced. All other off-diagonal elements are representing the various coherence orders. Each coherence elements has a real (r) and imaginary (s) part in it. Elements r_j and s_j, with $j = 1 \rightarrow 12$ representing the real and imaginary part of single quantum coherences. Whereas r_j and s_j, with $j = 13 \rightarrow 28$ representing the real and imaginary part of double, triple, or zero quantum coherences. Only single quantum coherences are directly accessible in NMR. As described in the 2-spin tomography method, we have to find suitable unitary transformations which can transfer the double, triple, zero, and population orders into single quantum coherences. Consider a propagator U, that transforms the original density matrix ρ into $\rho' = U\rho U^\dagger$. Following 13 unitary transformations were found to be sufficient to tomograph a three-spin homonuclear system.

(1). $\mathbb{1}$

(2). $\frac{1}{J_{13}}$

(3). $\frac{1}{2J_{13}}$

(4). $\frac{1}{J_{23}}$

(5). $\frac{1}{2J_{13}} \cdot 60_{90}$

(6). $\frac{1}{J_{13}} \cdot 90_{45}$

(7). $\frac{1}{2J_{13}} \cdot 90_{135}$

(8). $\frac{1}{2J_{13}} \cdot 45_{0}$

(9). $\frac{1}{J_{23}} \cdot 60_{45}$

(10). $\frac{1}{J_{13}} \cdot 45_{135}$

(11). $\frac{1}{2J_{13}} \cdot 30_{45}$

(12). $\frac{1}{J_{13}} \cdot 90_0 \cdot \frac{1}{2J_{13}} \cdot 90_0$

(13). $\frac{1}{2J_{13}} \cdot 60_{90} \cdot \frac{1}{J_{13}} \cdot 90_{135}$

Here $\mathbb{1}$ represents the identity operator i.e., direct observation without applying any extra pulses. J_{12}, J_{23}, and J_{13} are the scalar couplings between spin 1 & 2, spin 2 & 3, and spin 1 & 3 respectively (in Hz). The offset is assumed to be at the center of the spin-1 and spin-2 and the RF amplitudes are assumed to be much stronger than $\Delta\nu$. Hence, all the pulses used are non-selective RF pulses. For this particular case J_{12} is not used since it has very small coupling constant (a small coupling constant leads to larger duration of evolution which inturn makes the result more error prone).

Interms of unitary operator the delays ($\frac{1}{J_{13}}$ or $\frac{1}{J_{23}}$) can be written as bellow. For example, let us take the 2^{nd} experiment ($\frac{1}{J_{13}}$),

$$U_2 = e^{-i(H_j+H_{cs}).\frac{1}{J_{13}}}, \tag{5.2}$$

where, H_{cs} and H_j denoting Hamiltonian due to chemical shifts and J-couplings.

$$H_{cs} = \sum_{i=1}^{3} \nu_i I_z^i; \qquad H_j = \sum_{\substack{i=1 \\ i\neq j}}^{3} \sum_{j=1}^{3} 2\pi J_{ij} I_z^i I_z^j. \tag{5.3}$$

A combination of pulses and delays can also be seen as a required tomographic experiments. A pulse can be easily be written as a unitary transformation as shown in detail in previous appendix. For example, we can take the experiment named 60_{90} (experiment no. 5). The unitary operator for this pulse can be written as,

$$U_5 = e^{-i\frac{\pi}{3}(I_x^1+I_x^2+I_x^3)}. \tag{5.4}$$

We need to apply this unitary operator one by one on the primitive density matrix (B. 1). By doing individual integration on each of the transition (12 transition for each

experiment) and taking the imaginary values as well, we can get a total 312 linearly dependent equations. These equations can be solved by singular value decomposition (SVD) method and all the 63 unknowns can be find out.